Global and subtype-specific modulation of cortical inhibitory neurons regulated by acetylcholine during motor learning

Chi Ren[1], **Kailong Peng**[1,3], **Ruize Yang**[1,4], **Weikang Liu**[1], **Chang Liu**[2,5], **Takaki Komiyama**[1,6,*]

[1]Neurobiology Section, Center for Neural Circuits and Behavior, Department of Neurosciences, and Halıcıo lu Data Science Institute, University of California San Diego, La Jolla, CA 92093, USA

[2]Department of Computer Science and Engineering, University of California San Diego, La Jolla, CA 92093, USA

[3]Present address: Interdepartmental Neuroscience Program, Yale University, New Haven, CT 06520, USA

[4]Present address: Interdepartmental Neuroscience Program, Northwestern University, Chicago, IL 60611, USA

[5]Present address: Department of Bioengineering, University of California Berkeley, Berkeley, CA 94720, USA

[6]Lead contact

Summary

Inhibitory neurons (INs) consist of distinct subtypes with unique functions. Previous studies on INs mainly focused on single brain regions, and thus it remains unclear whether the modulation of IN subtypes occurs globally across multiple regions. Here, we monitored the activity of different cortical IN subtypes at both macroscale and microscale in mice learning a lever-press task. Learning evoked a global modulation of IN subtypes throughout the cortex. The initial learning phase involved strong activation of vasoactive intestinal peptide-expressing INs (VIP-INs) and weak activation of somatostatin-expressing INs (SOM-INs). Inactivating VIP-INs increased SOM-IN activity and impaired initial learning. Concurrently, cortical cholinergic inputs from the basal forebrain were initially more active but became less engaged over learning. Manipulation of the cholinergic system impaired motor learning and differentially altered activity of IN subtypes.

These results reveal that motor learning involves a global and subtype-specific modulation on cortical INs regulated by the cholinergic system.

eTOC blurb

With longitudinal calcium imaging at both macroscale and microscale in behaving mice, Ren et al. uncover a global and subtype-specific modulation of cortical inhibitory neuron activity regulated by the basal forebrain cholinergic system during motor learning.

Keywords

inhibitory neuron; cholinergic system; motor learning; wide-field calcium imaging; two-photon calcium imaging

Introduction

Cortical inhibitory neurons (INs) consist of heterogeneous populations, and each IN subtype carries out unique functions based on the morphological features, anatomical connectivity, and physiological properties (Hattori et al., 2017; Kepecs and Fishell, 2014; Tremblay et al., 2016). According to the expression of molecular markers, most cortical INs can be divided into three major subtypes: the vasoactive intestinal peptide- (VIP-), somatostatin- (SOM-), and parvalbumin- (PV-) expressing INs (Rudy et al., 2011). Even though each of these three subtypes includes heterogeneous subgroups (Tasic et al., 2018), they nevertheless represent largely distinct functional groups. PV-INs mainly target the perisomatic regions of excitatory neurons and inhibit their outputs, whereas SOM-INs typically synapse onto the distal dendrites and exert focal inhibition of synaptic inputs to excitatory neurons. In contrast, VIP-INs mostly inhibit other IN subtypes, mediating disinhibition of excitatory neurons (Letzkus et al., 2015; Markram et al., 2004; Naka and Adesnik, 2016). Such regulations by distinct IN subtypes are critical for shaping excitatory circuits in various brain functions during development and adulthood (Arriaga and Han, 2019; Bicks et al., 2020; Fu et al., 2014, 2015; Kim et al., 2016a; Krabbe et al., 2019; Kuchibhotla et al., 2016; Levelt and Hübener, 2012; Makino and Komiyama, 2015; Pi et al., 2013).

During motor learning, neural activity becomes more refined and reproducible both within the primary motor cortex (M1) and across spatially distributed cortical regions (Makino et al., 2017; Peters et al., 2014). Motor learning reorganizes local excitatory circuits in M1 layer 2/3 through the plasticity of dendritic spines at their distal dendrites (Chen et al., 2015b; Peters et al., 2014; Xu et al., 2009). It has been suggested that such learning-related spine reorganization is regulated by dendritic disinhibition from SOM-INs (Chen et al., 2015b). Other studies have also demonstrated that the proper functioning of SOM- and PV-INs is important to maintain learned motor skills (Adler et al., 2019; Cichon and Gan, 2015; Donato et al., 2013; Vallentin et al., 2016). Although accumulating evidence has suggested that different IN subtypes play unique roles in motor learning, these studies mainly focused on M1. Given that motor learning accompanies a reorganization of the cortex-wide activity in excitatory neurons (Makino et al., 2017), it is of particular interest to investigate whether learning also modulates IN subtypes globally throughout the cortex.

Furthermore, it remains elusive how individual IN subtypes are modulated from the initial learning phase to the expert stage. Additionally, the underlying mechanisms driving these subtype-specific modulations remain unclear.

To address these questions, we systematically monitored the activity of different cortical IN subtypes at both macroscale and microscale in mice learning a lever-press task. We found that different IN subtypes exhibited distinct learning-related changes in their activity during movements, not only in M1 but throughout the cortex. The IN subtype modulation was mediated by a strong engagement of cortical cholinergic inputs from the basal forebrain during the initial learning phase. Our results reveal a global, subtype-specific modulation of cortical INs regulated by the cholinergic system during motor learning.

Results

Global and subtype-specific modulation of IN activity in the dorsal cortex

To investigate the learning-induced dynamics of different IN subtypes throughout the cortex, we used motor learning as a platform and trained mice to learn a lever-press task (Peters et al., 2014) over weeks (n = 40 mice from session 1 to 21, n = 17 mice for session 22, one session per day, Figure 1A; STAR Methods). Using the same lever-press task, we have recently shown that motor learning evokes a reorganization of the cortex-wide macroscopic activity pattern in cortical excitatory neurons (Makino et al., 2017). In this task, water-restricted mice learned to use their left forelimb to press a lever beyond the set threshold during an auditory cue to receive a water reward. Mice showed a gradual improvement in performance over learning, indicated by the increased fraction of rewarded trials (p < 0.0001, mixed-effects model, Figure 1B). Furthermore, mice developed more reproducible lever-press movements with training (Figure 1C), as shown by the increased correlation of trial-by-trial lever trajectories both within (p < 0.0001, mixed-effects model) and across sessions (p < 0.0001, mixed-effects model, Figures 1D and 1E; see Figure S1 for other behavioral parameters and more example lever trajectories).

To monitor the cortex-wide activity of different IN subtypes, we performed longitudinal wide-field calcium imaging in task-performing mice with GCaMP6f expressed in VIP-, SOM-, or PV-INs broadly across the cortex (Figures 2A and S2A; STAR Methods). This was achieved by crossing VIP-Cre, SOM-Cre (Taniguchi et al., 2011), or PV-Cre mice (Hippenmeyer et al., 2005) with Cre-dependent GCaMP6f reporter transgenic mice (Madisen et al., 2015). Similar to the global activation of cortical excitatory neurons during movements (Makino et al., 2017; Musall et al., 2019), all three IN subtypes were activated during movements throughout the dorsal cortex during task performance (Figures 2B and S2B; Movie S1). The amplitudes of activity varied across regions with the largest amplitudes in regions that are most dorsal (e.g., S1HL). This pattern was similar to observations in wide-field calcium imaging of cortical excitatory neurons during the same lever-press task in our previous work (Makino et al., 2017) and also during the imaging of spontaneous activity (not shown). Therefore, amplitude differences across cortical regions may be of technical origin and so we limited our analysis to activity changes within each region. Additional control experiments using transgenic mice with GFP expressed in VIP-INs confirmed that

that the majority of fluorescence changes we report are indeed calcium signals (Figures S2C–S2F; STAR Methods).

To investigate the dynamics of IN subtypes during the learning of this motor task, we focused on the activity surrounding rewarded movements (STAR Methods). VIP- and SOM-INs demonstrated different changes in their activity during movement epochs. The activity of VIP-INs was initially strong and decreased in most of the cortical regions, while the activity of SOM-INs was initially weak and increased globally. In contrast, the activity of PV-INs was more stable in the dorsal cortex throughout learning, only showing a marginal increase in a minority of cortical regions (n (VIP) = 11 mice, n (SOM) = 12 mice, n (PV) = 11 mice, Figure 2C). We further characterized the changes in activity amplitude and duration by quantifying the peak and the full width at half maximum (FWHM) of trial-based IN activity in individual cortical regions respectively (STAR Methods). VIP-INs decreased the activity amplitude with learning while the activity duration remained stable. SOM-INs increased both the activity amplitude and duration (Figure S3). Therefore, motor learning evokes a global and subtype-specific modulation of IN activity in the dorsal cortex. The initial learning phase was accompanied by a strong global activation of VIP-INs and weak global activation of SOM-INs. We also note that, even though VIP- and SOM-INs changed their activity rather globally, there was also some heterogeneity across cortical regions. For example, the learning-related changes of VIP- and SOM-IN activity were strongly anti-correlated in M1, while VIP-IN activity remained relatively stable in RSC (Figure 2C).

To further evaluate the contributions of different behavioral events to neural activity during movement epochs, we constructed a generalized linear model (Musall et al., 2019; Pinto and Dan, 2015) to predict the activity of IN subtypes in each cortical region using a set of behavioral events as predictors (Figure 3A; STAR Methods). This model was able to closely reproduce the activity profile of three IN subtypes (Figures 3B–3D), predicting 47.98% ± 1.99%, 60.80% ± 1.40%, 59.92% ± 1.40% of variance in VIP-, SOM-, and PV-IN activity respectively (n (VIP) = 11 mice, n (SOM) = 12 mice, n (PV) = 11 mice, mean ± SEM). To determine the contributions of each behavioral event during movement epochs, we calculated the activity predicted by individual behavioral events by examining individual terms of the full model, and compared the predicted activity with the true imaged activity. Overall, the lever-press movements had the highest contribution to the activity, followed by licking, reward, and then the auditory cue (Figure 3E). Furthermore, the learning-related decreases of VIP-IN activity were driven by decreases in the activity related to lever-press movements, and increases of SOM-IN activity were attributed to lever-press movements and licking (Figure 3F). These results suggest that the activity and learning-related modulations that we report in this study are most strongly related to lever-press movements.

Modulation of individual VIP- and SOM-INs in M1 during motor learning

Wide-field calcium imaging monitors spatially integrated activity of neurons expressing the activity indicator. We further characterized the learning-induced dynamics of individual VIP- and SOM-INs, as these two subtypes showed more prominent modulations during learning in the wide-field experiments described above. The activity of layer 2/3 VIP- and SOM-INs in the right M1 was monitored longitudinally using two-photon calcium imaging

in task-performing mice (Figure 4A; STAR Methods). We injected adeno-associated viruses (AAV) encoding Cre-dependent GCaMP6f (AAV-Syn-FLEX-GCaMP6f) (Chen et al., 2013) into the forelimb area of the right M1 in VIP-Cre or SOM-Cre transgenic mice (Taniguchi et al., 2011). The forelimb area of the right M1 recorded in two-photon calcium imaging largely overlapped with the r-M1 module in wide-field calcium imaging. Individual VIP- and SOM-INs exhibited diverse activity profiles during movement epochs, displaying activated and suppressed responses during movements (870 VIP-INs from 7 mice, 533 SOM-INs from 10 mice, Figures 4B and 4G; STAR Methods). Consistent with the observations from wide-field calcium imaging, VIP- and SOM-INs displayed subtype-specific changes in their activity during learning, showing a decrease in the averaged population activity of VIP-INs ($p < 0.0001$, mixed-effects model, Figures 4C and 4D) but an increase of SOM-IN activity ($p = 0.0007$, mixed-effects model, Figures 4H and 4I). Consistently, at the single-cell level, the fraction of VIP-INs that significantly decreased their activity throughout learning was larger than those that increased (Early v.s. Naive: $p < 0.0001$, Middle v.s. Naive: $p < 0.0001$, Late v.s. Naive: $p < 0.0001$, mixed-effects model, corrected for multiple comparisons by false discovery rate, Figures 4E, 4F, and S4A). In contrast, the activity increased in a higher fraction of SOM-INs than the fraction of decreased SOM-INs (Early v.s. Naive: $p = 0.0011$, Middle v.s. Naive: $p = 0.0011$, Late v.s. Naive: $p = 0.0011$, mixed-effects model, corrected for multiple comparisons by false discovery rate, Figures 4J, 4K, and S4D). Given the diversity of activity of individual INs during movements (e.g., movement-activated vs. suppressed), we further investigated how the changes in the activity level during learning related to the types of activity during movements of individual neurons. In VIP-INs, the majority of neurons that decreased their activity were movement-activated at the naive stage but became less activated or non-modulated over learning (Figure S4C). In SOM-INs, neurons that increased their activity were mainly non-modulated at the naive stage but became movement-activated with learning (Figure S4F). Repeating the same analyses on the neurons from randomly selected 50% of animals consistently generated similar results (Figures S4B, S4C, S4E, and S4F), indicating that the phenomena we observed were not driven by a small number of outlier animals. Taken together, these results further demonstrate the subtype-specific modulation during motor learning at the cellular resolution. The activation of the majority of VIP-INs is strong at the beginning of learning and gradually decreases, while the activity of many SOM-INs is initially weak and increases during learning.

Inactivation of VIP-INs increases the SOM-IN activity during movements and impairs motor learning in naive animals

The strong activation of VIP-INs at the naive stage may allow learning-related plasticity of excitatory neurons by releasing them from SOM-IN inhibition (Chen et al., 2015b). To investigate the function of VIP-INs in the initial learning phase, we inactivated VIP-INs with hM4Di and CNO. CNO administration (10 mg/kg body weight) effectively inactivated VIP-INs during spontaneous lever-press movements (Figures S5A–S5C; STAR Methods). To further characterize the effective window of hM4Di under repeated CNO administrations during training, we expressed GCaMP6f in VIP-INs, with a subset of them also co-expressing hM4Di (Figure S5D; STAR Methods). This allowed us to compare the activity of hM4Di-expressing VIP-INs to non-hM4Di-expressing VIP-INs within the same

animal under CNO administrations. The inactivation was only effective in the first two CNO administrations (one administration per day, 10 mg/kg body weight, Figure S5E), possibly reflecting receptor desensitization and downregulation following repeated dosing with CNO (Roth, 2016). Therefore we restricted our experiments to the first two days of training, which correspond to the naive stage of learning.

We inactivated VIP-INs while monitoring the activity of SOM-INs in the right M1 with two-photon imaging during task performance in naive animals. This was achieved by using double transgenic mice in which the Cre recombinase was expressed in VIP-INs and the Flp recombinase was expressed in SOM-INs (VIP-Cre::SOM-Flp (He et al., 2016; Taniguchi et al., 2011)). We co-injected AAVs expressing Cre-dependent hM4Di (AAV-hSyn-DIO-hM4Di-mCherry) and Flp-dependent GCaMP6f (AAV-EF1a-fDIO-GCaMP6f) into the right M1 (hM4Di group, Figure 5A; STAR Methods). A cohort of animals expressing only mCherry in VIP-INs served as a control group (mCherry group, Figure 5A). With CNO administration, the SOM-INs were more strongly activated in the hM4Di group compared to the mCherry group (p = 0.0186, mixed-effects model, 619 neurons from 11 animals in the mCherry group, 559 neurons from 11 animals in the hM4Di group, Figures 5B–5E). The elevated activation of SOM-INs was still observed when we examined the neurons from randomly selected 50% of animals in each group (Figure S5F), indicating the consistency of the observation. Furthermore, the increased activation of SOM-INs during movements was accompanied by impairments in motor learning. Naive animals in the hM4Di group showed a lower fraction of rewarded trials and a longer time interval from movement onset to reward (mixed-effects model, 11 animals in each group, Figure 5F). These impairments in task performance were unlikely due to reduced motivation or deficits in movement generation (Figure S5G). In addition, animals in the hM4Di group also performed worse at the beginning of the session after CNO manipulation sessions compared to the control group (Figure 5G), suggesting a deficit from poor learning in prior CNO manipulation sessions. These results suggest that the strong activation of VIP-INs at the naive stage of learning suppresses SOM-INs, creating a window for learning-related plasticity in excitatory neurons and allowing the acquisition of new motor skills.

Strong activation of basal forebrain cholinergic projections to the cortex in the initial learning phase

What is the mechanism underlying the globally-orchestrated, subtype-specific dynamics of INs during motor learning? We hypothesized that the basal forebrain cholinergic system could mediate these changes based on the following reasons. In a subset of animals, we performed pupillometry recordings and observed a large pupil dilation during movements in the initial learning phase that decreased with learning (Figures S6A and S6B; STAR Methods). As the pupil diameter correlates with noradrenergic and cholinergic activity in the cortex (Reimer et al., 2016), the changes in pupil dilation suggest the involvement of neuromodulators, including acetylcholine (ACh), during learning. Previous literature has also supported the role of ACh in mediating learning-related modulations of IN activity. First, the basal forebrain cholinergic system is widely implicated in learning (Crouse et al., 2020; Guo et al., 2019; Lin et al., 2015). Second, cortical INs express ACh receptors (AChRs) and are responsive to cholinergic inputs (Dasgupta et al., 2018; Fu et al., 2014;

Gasselin et al., 2021; Kuchibhotla et al., 2016; Yao et al., 2021). Third, basal forebrain cholinergic neurons project broadly to the cortex (Do et al., 2016; Kim et al., 2016b; Li et al., 2018; Woolf, 1991), which may drive the global changes in IN activity during learning.

To monitor the dynamics of basal forebrain cholinergic inputs to the cortex during motor learning, we injected AAV-hSyn-FLEX-axon-GCaMP6s (Broussard et al., 2018) into the basal forebrain of ChAT-Cre transgenic mice (Rossi et al., 2011) and recorded the activity of cholinergic axons in the cortex with two-photon calcium imaging during learning (Figures 6A, 6B, and S6C–S6E; STAR Methods). We imaged the right M1, S1HL, and PPC in separate sessions to cover a range of areas across the dorsal cortex. In all three cortical regions, the activation of cholinergic axons during movements was most prominent at the naive stage, which then was gradually attenuated with learning (p (M1) = 0.0016, p (S1HL) = 0.0059, p (PPC) = 0.0190, mixed-effects model, n (M1) = 7 mice, n (S1HL) = 6 mice, n (PPC) = 6 mice, Figure 6C), suggesting a global learning-related modulation in which the cholinergic projections are highly recruited across distributed cortical regions in naive but less engaged in expert mice. This observation is consistent with the decreased pupil dilation during learning (Figure S6B) and shows a similar trend as the decreased VIP-IN activity with learning (Figures 2 and 4).

Basal forebrain cholinergic inputs to the cortex are necessary for efficient motor learning

Having established that the cholinergic projections are particularly active during the initial learning phase, we next asked whether the cholinergic system contributed to the learning of new motor skills. To test this idea, we used two different methods to impair the cholinergic system and examined the effect on behavior. First, we ablated basal forebrain cholinergic neurons bilaterally by injecting AAV-EF1a-FLEX-taCaspase3 (Yang et al., 2013) into the basal forebrain of ChAT-Cre mice (STAR Methods). A separate cohort of ChAT-Cre animals receiving saline injections served as a control group (Figure 6D). Four weeks after injections, histological analyses revealed that this approach achieved a nearly complete ablation of cholinergic neurons restricted to basal forebrain nuclei (Figures S7A–S7F). Compared to the control group, mice in the ablation group showed deficits in learning the lever-press task. The ablation animals were slower in achieving high success rates, and their movements did not reach the same level of reproducibility as control animals (n (Ablation) = 15 mice, n (Control) = 13 mice, Figures 6E, 6F; see Figure S7G for other behavioral parameters).

Chronic ablation of cholinergic neurons could induce compensatory mechanisms that limit behavioral effects. Additionally, because basal forebrain cholinergic neurons also send projections to subcortical regions, the behavioral effects above could originate from cholinergic functions in subcortical regions. To address these issues, we also performed a cortex-wide and acute ontogenetic inactivation targeting basal forebrain cholinergic projections to the cortex using the inhibitory opsin eOPN3 (Mahn et al., 2021). Activating eOPN3 with green light (~532 nm, ~2 mW/mm^2 for 15 s) reduced GCaMP6f responses by ~50% in cholinergic axons (Figures S7H–S7J; STAR Methods). This is a larger degree of suppression than the results reported in the original paper (Mahn et al., Neuron, 2021), suggesting an effective (but not complete) suppression of the cholinergic activity with

eOPN3. To achieve a cortex-wide inactivation of the basal forebrain cholinergic projections, we bilaterally injected AAV-hSyn-SIO-eOPN3-mScarlet in the basal forebrain of ChAT-Cre animals (eOPN3 group, Figure 6G; STAR Methods). A separate cohort of ChAT-Cre animals received injections of AAV-hSyn-DIO-mCherry and served as a control group (mCherry group). Green light was delivered to the entire dorsal cortex through the skull (~532 nm, ~4 mW/mm^2 at the skull surface and ~2 mW/mm^2 at the brain surface, for 15 s every 5 min spanning entire sessions, Figures S7I and S7J; STAR Methods) in both groups during training. Compared to the control group, the eOPN3 group showed a lower fraction of rewarded trials at the early stage of learning (Figure 6H, n (eOPN3) = 9 mice, n (mCherry) = 8 mice). Furthermore, the lever-press movements of eOPN3 group were less reproducible (Figure 6I, see Figure S7K for other behavioral parameters). Given the incomplete inactivation by eOPN3, the results are lower-bound estimates of the true effects of cholinergic signaling in learning.

These results suggest that cholinergic projections to the cortex play an important role in the acquisition of new motor skills. Then, could the behavior be improved by artificially elevating cortical cholinergic activity? To test this idea, we bilaterally injected AChR agonists (3 μM nicotine and 0.5 mM carbamoylcholine chloride) into M1 in naive animals and trained them with the lever-press task (STAR Methods). This elevation of cholinergic signaling in M1 improved task performance and led to a significant increase in the fraction of rewarded trials (Figure 6J, n (Ago.) = 5 mice, n (Sal.) = 5 mice). Other measures of task performance were not significantly altered. Thus, even though the observed effect is mild, this result implies that cholinergic activity in normal mice during the initial stage of learning is not saturated. Rather, it is possible to facilitate initial learning by artificial activation of cholinergic signaling.

Manipulation of cholinergic signaling alters the activity during movements of VIP- and SOM-INs in motor learning

The learning-related dynamics observed in IN subtypes and cholinergic inputs to the cortex are consistent with a simple circuit model that modulates the gain and plasticity of visual cortex neurons during locomotion (Fu et al., 2014, 2015). Our results suggest that this mechanism is engaged globally across cortex during motor learning (Figure 7A). At the initial stage of learning, the cholinergic system is highly active during movements, driving a strong activation of VIP-INs, which in turn inhibit SOM-INs. With learning, the cholinergic system becomes less engaged. The decreased excitation from cholinergic inputs attenuates VIP-IN activity, allowing a stronger activation of SOM-INs during movements. This model could be a mechanism behind our previous observation that decreased inhibition from SOM-INs to excitatory neurons during learning enhances excitatory neuron plasticity and permits motor learning (Chen et al., 2015b).

To examine whether the cholinergic system modulates the activity of IN subtypes during motor learning, we pharmacologically manipulated cholinergic signaling in the right M1, while imaging the activity of VIP- and SOM-INs in both naive and expert animals. According to the model above, artificially suppressing the cholinergic system in naive mice should decrease and increase the activity of VIP-INs and SOM-INs during movements,

respectively. In contrast, boosting cholinergic signaling in expert mice should elevate and suppress the activity of VIP-INs and SOM-INs, respectively.

To test the first prediction, we injected a cocktail of AChR antagonists (3 mM mecamylamine and 100 μM atropine) into the right M1 in one training session during the first two days of training (STAR Methods). Antagonist sessions and control sessions were alternated across animals to balance the potential learning effects on neural activity in both groups. At the naive stage, blocking cholinergic signaling with AChR antagonists significantly decreased the activity of VIP-INs (p = 0.0024, mixed-effects model, 775 VIP-INs from 10 mice, Figures 7B–7F) and increased the activity of SOM-INs (p = 0.0062, mixed-effects model, 1128 SOM-INs from 11 mice, Figures 7G–7K), consistent with our prediction. Similar to the changes during learning, the majority of VIP-INs with decreased activity were movement-activated in the control session and became non-modulated with the application of AChR antagonists (Figure S8B). In SOM-INs, most neurons showing increased activity were previously non-modulated during movements but became activated with AChR antagonists (Figure S8D). Concurrent with the alteration of IN activity, blocking cholinergic signaling also mildly impaired learning at the naive stage, resulting in a lower fraction of rewarded trials (Figure S8I).

We further examined the roles of different AChR subtypes in mediating the modulation of VIP-IN activity in naive mice by applying nicotinic AChR (nAChR) antagonist (3 mM mecamylamine) and muscarinic AChR (mAChR) antagonist (100 μM atropine) in separate groups of animals. Applying nAChR antagonist alone significantly reduced the activity of VIP-INs during movements (Figures 7L–7P), which largely recapitulated the effects of injecting a cocktail of nAChR and mAChR antagonists (Figures 7B–7F). In contrast, mAChR antagonist did not robustly reduce the VIP-IN activity (Figures 7Q–7U), suggesting that cholinergic signaling acts on VIP-INs mainly through nAChRs.

To test the second prediction, we activated cholinergic signaling in the right M1 with AChR agonists (3 μM nicotine and 0.5 mM carbamoylcholine chloride) in expert mice. This manipulation altered the activity of INs during movements in the direction opposite to the antagonist experiments in naive animals above. Applying AChR agonists significantly increased the activity of VIP-INs (p = 0.0063, mixed-effects model, 995 VIP-INs from 11 mice, Figures 8A–8E) and decreased the activity of SOM-INs during movements (p = 0.0166, mixed-effects model, 762 SOM-INs from 10 mice, Figures 8F–8J). The majority of VIP-INs showing increased activity were non-modulated in expert mice but became activated during movements with AChR agonists (Figure S8F), and the majority of SOM-INs with decreased activity were movement-activated but became non-modulated with cholinergic activation (Figure S8H). Repeating the same analyses on the neurons pooled from randomly selected 50% of animals generated similar results (Figures S8A–S8H), indicating that the results are consistent across animals. We noticed that applying AChR agonists slightly increased the movement stereotypy in expert animals (Figure S8J). This result is similar to an observation in songbirds (Jaffe and Brainard, 2020) and suggests that ACh may reduce the variability of the activity of the motor cortex during well-learned movements. Taken together, these results support our model (Figure 7A) and demonstrate

that the movement-related dynamics of cortical IN subtypes are modulated by cholinergic inputs during motor learning.

Discussion

Previous studies have revealed distinct roles of IN subtypes in M1 during motor learning (Adler et al., 2019; Chen et al., 2015b; Cichon and Gan, 2015; Donato et al., 2013). Here, we extended these studies by systematically monitoring the activity from IN subtypes at both macroscale and microscale throughout motor learning. Equipped with the large-scale activity monitoring with wide-field calcium imaging, we found that motor learning induced subtype-specific changes in IN activity throughout the cortex. The initial phase of learning accompanied high activity of VIP-INs and low activity of SOM-INs during movements. As various task events temporally overlapped, such as the auditory cues, lever-press movements, and rewards, we constructed a generalized linear model to dissect the contributions of individual behavioral events to neural dynamics. Although this is a common approach utilized in many recent studies, a more complex task design with a better temporal separation between task events could further clarify the relationships between behavioral events and dynamics of IN subtypes during learning.

VIP-INs have been demonstrated to be critical in state-dependent modulation and associative learning by suppressing other IN subtypes, mediating disinhibition on excitatory neurons (Donato et al., 2013; Fu et al., 2014, 2015; Gasselin et al., 2021; Krabbe et al., 2019; Letzkus et al., 2015; Pi et al., 2013; Zhang et al., 2014). Our results suggest that a similar disinhibition mechanism is also adopted in motor learning and this occurs globally throughout the cortex. Due to the limited effective window of DREADD, we only assessed the function of VIP-INs in the initial learning phase. Other manipulation methods that can achieve more extended periods (e.g., optogenetics) will be beneficial to study the function of VIP-INs in developing behavioral features requiring long-term training (e.g., movement reproducibility).

The selective disinhibition through SOM-INs could arise from a preferential connection from VIP-INs to SOM-INs in cortical circuits (Lee et al., 2013; Pfeffer et al., 2013; Pi et al., 2013). This aligns with the previous observation that learning-induced spine plasticity is largely restricted to the apical dendrites of M1 excitatory neurons, the dendritic compartment inhibited by SOM-INs (Chen et al., 2015b). However, we note that the modulation of IN activity happened immediately at the beginning of learning, while the structural plasticity occurred more gradually over days (Chen et al., 2015b). The dissociation of timing between the activity modulation and structural plasticity suggests that multiple disinhibitory mechanisms contribute to a sequential regulation of plasticity. The rapid activity modulation of INs may play a permissive role in broadly opening the plasticity window, while the slower structural plasticity of INs may provide more targeted signals by relying on the interactions with individual excitatory neurons (Bloodgood et al., 2013; Xue et al., 2014) and neighboring astrocytes (Allen and Eroglu, 2017).

It should be noted that our two-photon calcium imaging experiments focused on layer 2/3, and so the learning-related modulation of INs in deeper layers remains unclear. It has been

shown that SOM-INs are heterogeneously modulated in different cortical layers (Munoz et al., 2017), suggesting that a layer-specific modulation may also occur during learning. We noticed that wide-field signals of SOM-INs continued to increase throughout learning but their two-photon signals appeared to plateau earlier (Figure 2C compared to Figure 4I). As wide-field signals also contain the activity of layer 1 axons from SOM-INs in deep layers (Jiang et al., 2015; Nigro et al., 2018), the prolonged changes of wide-field signals could implicate a more gradual modulation of SOM-INs in deep layers. Future studies are required to directly examine the learning-related modulation of INs in different cortical layers.

Concurrent with the changes in cortical INs, the basal forebrain cholinergic projections to the cortex were particularly active in the initial learning phase. Such learning-related modulation on the basal forebrain cholinergic system may reflect a global state change when animals are engaged in a new task. The basal forebrain cholinergic neurons are rapidly recruited by reinforcement signals (Hangya et al., 2015). Therefore, the global modulation of cortical INs may not be unique to motor learning but generally occur in various forms of learning. The strength of such global modulation may depend on the exact learning paradigms and cognitive demands of the tasks. Furthermore, recent studies have pointed out the heterogeneity of the projection targets of individual cholinergic neurons (Kim et al., 2016b; Li et al., 2018) and the cortex-wide cholinergic signaling in spontaneous activity (Lohani et al., 2020). Directly characterizing the cortex-wide cholinergic activity with simultaneous large-scale recordings during task engagement will be of particular interest in future studies.

To determine the contributions of cholinergic inputs to motor learning, we used two different methods to impair the cholinergic system. We note that both manipulation methods have their own caveats: chronic ablation could induce compensatory mechanisms, and optogenetic inactivation with eOPN3 is likely incomplete. Therefore, the results probably underestimate the true effects of cholinergic signaling in learning. Nevertheless, we observed robust impairments in motor learning from different manipulation methods applied to the basal forebrain cholinergic system, suggesting basal forebrain cholinergic inputs to the cortex play an important role in learning new motor skills. Furthermore, the deficits in developing movement reproducibility caused by the lack of cholinergic inputs recapitulate the behavioral effects of M1 lesion before training in the same lever-press task (Peters et al., 2014).

Manipulation of cholinergic signals also affected IN activity both in the initial and expert learning phases, suggesting the involvement of cholinergic signaling in modulating IN activity during motor learning. While the current study focused on the net effect of cholinergic inputs on IN activity during motor learning, ACh can act directly on nearly every type of cortical neurons through both mAChRs and nAChRs (Colangelo et al., 2019; Rudy and Munoz, 2014; Yao et al., 2021). Therefore, ACh likely acts at multiple loci in cortex during learning, including both direct effects on INs and indirect modulation through networks. For example, cholinergic inputs can excite VIP-INs through at least 3 mechanisms: via direct depolarization through AChRs on VIP-INs (Arroyo et al., 2012; Chen et al., 2015a), by enhancing excitatory presynaptic inputs onto VIP-INs (Lee et al., 2013; Williams and Holtmaat, 2019; Zhang et al., 2014), and by suppressing other IN

subtypes that inhibit VIP-INs (Karnani et al., 2016; Zhang et al., 2014). Furthermore, the cholinergic system can also modulate excitatory neurons (Colangelo et al., 2019) and thalamocortical inputs (Kruglikov and Rudy, 2008). Besides the strong VIP-IN activation, the high activity of cholinergic inputs in the initial learning phase may also suppress the recurrent cortical activity and enhance thalamocortical inputs (Hasselmo and Sarter, 2011). All these ACh-mediated modulations may work together to facilitate the integration of task-relevant information in the cortex (Ballinger et al., 2016; Minces et al., 2017). Thus, it is likely that the cholinergic system contributes to motor learning not only through the modulation of VIP-INs but through the regulation of various circuit components. A more comprehensive understanding of how cholinergic signaling modulates the circuit dynamics could be aided by computational models of cortical circuits with detailed characterization of the expression pattern of AChRs in each circuit component (Ramaswamy et al., 2018; Saunders et al., 2018; Zeisel et al., 2018). In addition to the cholinergic system, a mixture of different inputs, such as other neuromodulators (Hattori et al., 2017) and long-range inputs from other brain regions (Ährlund-Richter et al., 2019; Makino and Komiyama, 2015; Wall et al., 2016; Williams and Holtmaat, 2019; Zhang et al., 2014), can drive the learning-related modulation in cortical INs. A detailed anatomical and functional characterization of inputs to IN subtypes will help complete the picture of underlying mechanisms.

Neuromodulatory control of IN subtypes likely subserves a signal to open the temporal window of plasticity for excitatory circuits. The global nature of this signaling makes it unlikely for this mechanism to provide the spatial specificity with regards to which synapses in which brain regions become plastic. However, we note that motor learning evokes a reorganization of cortex-wide macroscale activity patterns of excitatory neurons (Makino et al., 2017). Therefore, motor learning probably involves spatially distributed synaptic reorganizations, and the global signaling described in this study may be best suited to allow temporal coordination of plasticity across spatial scales. Furthermore, we acknowledge that the behavioral effects of various manipulations in this study are relatively mild, slowing learning rather than blocking it completely. We believe that the mechanisms we describe here modulate the degree of learning rather than serving as a binary gating switch.

Taken together, our results reveal a global and subtype-specific modulation on cortical INs regulated through the cholinergic system during motor learning, and provide insights into how different IN subtypes contribute to learning-induced reorganization in excitatory circuits.

STAR Methods

RESOURCE AVAILABILITY

Lead Contact—Further information and requests for resources, reagents, and data should be directed to and will be fulfilled by the lead contact Takaki Komiyama (tkomiyama@ucsd.edu).

Materials Availability—This study did not generate new unique reagents.

Code and Data Availability—Analyzed data have been deposited at Mendeley Data (DOI: 10.17632/tcnk38zkyz.1) and are publicly available as of the date of publication. The DOI is also listed in the key resources table. The raw data are too large to be deposited in a public repository, but will be shared by the lead contact upon request.

The custom MATLAB codes have been deposited at https://github.com/CRen2333/InhibitoryNeuron_LeverPress.git and the link is also listed in the key resources table.

Any additional information required to reanalyze the data reported in this paper is available from the lead contact upon request.

EXPERIMENTAL MODEL AND SUBJECT DETAILS

Mouse lines—All procedures were performed following protocols approved by the UCSD Institutional Animal Care and Use Committee and guidelines of the National Institute of Health. Mice were acquired from Jackson laboratories, including PV-Cre [JAX:017320], SOM-Cre [JAX:013044], VIP-Cre [JAX:010908], SOM-Flp [JAX:028579], Ai95 [JAX:024105], and ChAT-Cre [JAX:006410], and used to generate double transgenic mice. Mice were group-housed in disposable plastic cages with standard bedding in a room with a reversed light cycle (12 h-12 h). Experiments were performed during the dark period. Both male and female healthy adult mice (6 weeks or older) were used. Mice had no prior history of experimental procedures that could affect the results. For manipulation experiments, littermates were randomly assigned to experimental and control groups.

METHOD DETAILS

Surgeries and virus injections

For two-photon calcium imaging: Surgical procedures were performed as previously described (Peters et al., 2014). Adult mice (6 weeks or older, male and female) were anesthetized with 1%-2% isoflurane and injected with Baytril (10 mg/kg), dexamethasone (2 mg/kg), and buprenorphine (0.1 mg/kg) subcutaneously at the beginning of surgery to prevent infection, inflammation, and discomfort. A custom-built head-plate was glued and cemented to the skull. For imaging cholinergic projections in the right S1HL and PPC, a large hexagonal craniotomy (~6×5.5 mm) was performed to encompass both cortical regions. For other two-photon imaging experiments, craniotomy (~3 mm in diameter) was performed over the right caudal forelimb area (0.3 mm anterior and 1.5 mm lateral from the bregma).

For injections within the right M1, virus solutions were injected around the center of the caudal forelimb area at 5 sites (~250 μm deep, ~500 μm apart). Pipettes were left in the brain for 4-5 min after each injection to avoid backflow. For imaging cortical IN subtypes, virus solutions of AAV-Syn-FLEX-GCaMP6f were injected with 30-40 nL at each site over ~3 min in respective Cre lines. For confirming the effectiveness of hM4Di in VIP-INs, virus solutions of AAV-hSyn-DIO-hM4Di-mCherry and AAV-Syn-FLEX-GCaMP6f at a titer ratio of 1:1 were injected with 200 nL at each site over ~10 min in VIP-Cre mice. For characterizing the effectiveness window of hM4Di under repeated dosing of CNO, virus solutions of AAV-hSyn-DIO-hM4Di-mCherry and AAV-Syn-FLEX-GCaMP6f at a

titer ratio of 1:5 were injected with 200 nL at each site over ~10 min in VIP-Cre mice. This mixture ratio was to achieve co-expression of hM4Di only in a subset of GCaMP6F-expressing VIP-INs. For the manipulation of VIP-IN activity with simultaneous imaging of SOM-INs, virus solutions of AAV-hSyn-DIO-hM4Di-mCherry (AAV-hSyn-DIO-mCherry in control animals) and AAV-EF1a-fDIO-GCaMP6f were injected with 200 nL at each site over ~10 min in VIP-Cre::SOM-Flp mice. A cohort of animals that were littermates of the hM4Di group received injections of virus solutions of AAV-hSyn-DIO-mCherry and AAV-EF1a-fDIO-GCaMP6f and served as a control group. The surgical procedures were identical between two groups.

For imaging cholinergic projections to the cortex, virus solutions of AAV-hSyn-FLEX-axon-GCaMP6s were injected in the basal forebrain with ~1 μL virus solutions per hemisphere over ~10-15 min and pipettes were left in the brain for 10 min after each injection to minimize backflow. For imaging cholinergic projections to the right M1, virus solutions were injected through angled injections in ChAT-Cre mice to avoid inserting the pipette directly through the right M1 and infecting local ChAT+ neurons by backflow. Pipettes were inserted through small craniotomies (~0.5 mm) around 2.0 mm posterior and 1.7 mm lateral from the bregma at 18° relative to the vertical plane, and the pipette tips targeted the region around 0.3 mm posterior and 1.7 mm lateral from the bregma and 4.75 mm deep from the brain surface. For imaging cholinergic projections to the right S1HL and PPC, pipettes were inserted vertically through small craniotomies (~0.5 mm) around 0.3 mm posterior and 1.7 mm lateral from the bregma to 4.75 mm deep from the brain surface.

For confirming the effectiveness of eOPN3, ~1.8 μL virus solutions of 50:50 mixtures of AAV-hSyn-SIO-eOPN3-mScarlet and AAV-hSyn-FLEX-axon-GCaMP6s were injected in the right basal forebrain through angled injections, as described above.

After virus injections, a glass window was implanted over the craniotomy. The edges between the window and the skull were filled with Vetbond (3M). The window was further secured with cyanoacrylate glue and dental acrylic. For imaging IN subtypes, experiments were performed ~3-4 weeks after surgery. For imaging cholinergic axons, experiments were performed ~5-8 weeks after surgery. For test the effectiveness of eOPN3, experiments were performed ~7 weeks after surgery.

For wide-field calcium imaging: Adult mice (6 weeks or older, male and female) were anesthetized with 1%-2% isoflurane and injected with Baytril (10 mg/kg), dexamethasone (2 mg/kg), and buprenorphine (0.1 mg/kg) subcutaneously at the beginning of surgery. A custom-built head-bar was glued and cemented to the skull (~1 mm posterior to lambda). To improve the signal-to-noise ratio limited by the relatively low density of each IN subtype, we replaced most of the dorsal skull with a curved transparent glass window (Kim et al., 2016c). A large craniotomy was performed to remove most of the dorsal skull. A curved glass window consisting of a hexagonal glass plug (~8 × 7 mm) and a base (~10 × 8.5 mm) was implanted over the craniotomy. The edges between the window and the skull were filled with Vetbond. The window was secured with cyanoacrylate glue and dental acrylic. A custom-designed 3D-printed hexagonal crown (~10 mm × 10 mm) was glued to the

circumference to protect the window and minimize the entry of the excitation light to the eyes during imaging. Experiments were performed ~4 weeks after surgery.

For ablation of basal forebrain cholinergic neurons: Adult ChAT-Cre mice (6 weeks or older, male and female) were anesthetized with 1%-2% isoflurane and injected with Baytril (10 mg/kg), dexamethasone (2 mg/kg), and buprenorphine (0.1 mg/kg) subcutaneously at the beginning of surgery. Virus solutions of AAV-EF1a-FLEX-taCaspase3 were injected bilaterally to the basal forebrain through angled injections, as described above. ~1 μL virus solutions were injected over ~10-15 min on each side. After injections, the craniotomies were sealed with Vetbond. A custom-built head-bar was glued and cemented to the skull (~1 mm posterior to lambda), and the exposed skull was covered by cyanoacrylate glue and dental acrylic. Experiments were performed ~4-5 weeks after surgery. Saline was similarly injected in control animals that were littermates of the ablation group and the surgical procedures were identical to the ablation group.

For inactivation of basal forebrain cholinergic projections to the cortex with eOPN3: Surgical preparations were identical to the preparations for ablation of basal forebrain cholinergic neurons. Virus solutions of AAV-hSyn-SIO-eOPN3-mScarlet were injected bilaterally to the basal forebrain through angled injections in adult ChAT-Cre mice (6 weeks or older, male and female). Virus solutions of AAV-hSyn-DIO-mCherry were similarly injected in control animals that were littermates of the ablation group. ~1 μL virus solutions were injected over ~10-15 min on each side. Experiments were performed ~7 weeks after surgery. ~2 days before the training started, a ring of black heat shrink tube (~5 mm in height, ~2 cm in diameter) was glued to the circumference of the skull to minimize the entry of the green light (~532 nm) to the eyes during optogenetic inactivation. Experiments were performed ~7 weeks after surgery.

Behavior—Water restriction started 2 weeks before the behavioral training at 1 mL per day. After water restriction, mice were trained to perform the lever-press task 1 session per day for ~3 weeks under a microscope (21 days for wide-field calcium imaging and 22 days for two-photon calcium imaging). The hardware and software used for behavioral training have been previously described (Peters et al., 2014). In brief, a 6 kHz tone marked a cue period (up to 10 s), during which a successful lever press was rewarded with water (~10 μL per trial) paired with a 500 ms, 12 kHz tone, and followed by an inter-trial interval (ITI, variable duration of 8-12 s). Licking was monitored using an infrared lickometer (Island Motion Co.). A successful lever-press movement was defined as crossing two thresholds (~1.5 mm and ~ 3.375 mm below the resting position) within 200 ms. Failure to press the lever passing the two thresholds during the cue period triggered a loud white-noise sound and the start of an ITI. Lever presses during ITIs were neither rewarded nor punished. In two-photon calcium imaging, each session consisted of around 100 trials. In wide-field calcium imaging, each session consisted of 80–150 trials and was terminated when mice reached 80 successful trials or performed 150 trials, whichever came first. Sessions were binned into 4 stages in analyses (naive: sessions 1-2; early: 3-8; middle: 9-16; late: 17-22 for animals under two-photon imaging and 17-21 for animals under wide-field imaging). To

examine the effects of ablating basal forebrain cholinergic neurons, both ablation and control groups performed 100 trials per session for 21 days.

For chemogenetic inactivation experiments, Clozapine-N-Oxide (CNO, Enzo Life Sciences) was dissolved in deionized water to a 2.5 mg/mL concentration and injected intraperitoneally at a 10 mg/kg body weight dose 30 min before behavioral training.

For the following manipulation experiments, including chemogenetic inactivation of VIP-INs, ablation of basal forebrain cholinergic neurons, optogenetic inactivation of cholinergic projections to the cortex, and pharmacological activating cholinergic signaling in naive mice, the training procedures were identical between the manipulation and control groups, and littermates belonging to two groups were trained in parallel on the same days.

Lever-press movement analysis—Lever traces were processed and movement bouts were identified as previously described (Peters et al., 2014). In brief, lever traces were downsampled from 10 kHz to 1 kHz and filtered with a low-pass Butterworth filter (4-pole 10 Hz). Movement bouts were detected by a velocity threshold (4.9 mm/s) using the filtered lever traces, and the onset and offset of movement bouts were refined by the lever position leaving or entering the resting period, respectively. Cued trials were defined as the trials with an at least 100-ms movement-quiescent period preceding the cue onset. Only rewarded movements in the cued trials were included in further analyses. Lever trajectories for these movements were collected from 0-2 s relative to the movement onset, which was approximately the duration of rewarded movements for all animals (2.19 ± 0.18 s, mean $\pm$ SEM). The similarity of lever trajectories across trials was computed by Pearson correlation (Figures 1D, 1E, 5F, 6F, 6I, 6J, S8I, and S8J).

Licking analysis—Licking bouts were identified as previously described (Komiyama et al., 2010). In brief, licking bouts were defined as no less than three continuous licks with inter-lick intervals < 300 ms. The licking bout onsets were defined as the start of individual licking bouts (Figure 3).

Imaging data acquisition

For two-photon calcium imaging: For cortical INs, imaging was conducted with a commercial two-photon microscope (MOM, Sutter Instrument, retrofitted with a resonant galvanometer-based scanning system from Thorlabs), $16 \times$ objective (Nikon), and 925 nm excitation light (Ti:Sapphire laser, Newport) controlled by ScanImage (Vidrio Technologies). Images were recorded at ~28 Hz continuously, alternating between 2 depths within layer 2/3. At each depth, images were acquired at ~14 Hz with a field of view of ~590×635 μm with 512×512 pixels. Imaging was alternated between two locations in the right M1 each day such that each field was imaged every other day. For basal forebrain cholinergic projections to the right M1, images were acquired using a commercial two-photon microscope (B-Scope, Thorlabs) at ~30 Hz with a field of view of ~204×220 μm with 512×512 pixels in layer 1. For basal forebrain cholinergic projections to the right S1HL and PPC, the two fields of view were alternated between imaging sessions within the same animal. To minimize photobleaching and phototoxicity, at the early and middle stages of learning, axonal imaging was only performed in the middle two sessions within each stage. Frame

times were recorded and synchronized with behavioral recordings by the Ephus software. Slow drifts in the field of view were manually corrected using reference images during imaging.

For wide-field calcium imaging: Wide-field calcium imaging was performed using a commercial fluorescence microscope (Axio Zoom.V16, Zeiss, objective lens (1 ×, 0.25 NA)) and a CMOS camera (ORCA-Flash4.0 V2, Hamamatsu) as previously described (Makino et al., 2017). The light source for wide-field calcium imaging was HXP 200 C (Zeiss). The filter set (000000-1021-600, Zeiss) for imaging GCaMP signals consisted of a bandpass filter for the excitation light (485 ± 17 nm), a beamsplitter (500 nm), and a tunable bandpass filter centered at 520 nm for the emission light. Images were acquired using HCImage Live (Hamamatsu) at 29.98 Hz, 512 × 512 pixels (field of view: ~8.5 × 8.5 mm, binning: 4, 16 bit) every other session of behavioral training. Each session consisted of several 5-min blocks, and every other block was imaged to minimize photobleaching. Imaging and behavioral data were acquired simultaneously and aligned off-line based on a synchronization signal.

Two-photon imaging analysis

ROI identification and fluorescence analysis: Images were first aligned frame-by-frame using a custom MATLAB program to correct lateral movements and distortions (Hattori and Komiyama, 2021; Mitani and Komiyama, 2018). For cortical INs, ROIs were manually drawn and aligned across sessions using a custom MATLAB program (Peters et al., 2014) by visual inspection. ROIs showing a filled nucleus by GCaMP6f were excluded from all analyses. A ring-shaped 'background ROI' containing neuropil signals was created from the border of each neuronal ROI to a width of 6 pixels. For cholinergic axons, ROIs were first identified with Suite2P (Pachitariu et al., 2016) and then selected with visual inspection. ROIs clearly belonging to the same axon were manually combined. For each field of view, three background ROIs were manually drawn in the dark area without obvious fluorescent transients. Their averaged fluorescence time series was used as the background fluorescent trace for all axonal ROIs in the same field of view.

Fluorescence analysis was processed as described (Peters et al., 2014). Briefly, pixels within each ROI were averaged to create a fluorescence time series, and the background fluorescent trace was subtracted. To estimate the time-varying baseline (f) of a fluorescence trace, the raw fluorescence trace was smoothed with a 4-min moving average window, and f was estimated based on the inactive portions of the trace.

Classification of neurons showing significant changes in their activity during movements: The mean activity from 0 s to 2 s after movement onset in each trial, after subtraction of the baseline (the averaged activity between −357 ms and −214 ms relative to the movement onset) was used as activity during movements for comparison (Figures 4, 5B–5E, 7, 8, S4, S5B, S5C, S5E, and S8). To determine whether a given neuron significantly changed its activity during movements with learning, the trials from the early, middle, or late stage were pooled with trials from the naive stage, forming an activity dataset. The trial identity in the dataset was shuffled 1,000 times and generated a null distribution of

the activity change relative to the naive stage. If the actual activity change fell in the left (< 2.5%) or the right (> 97.5%) tail of the null distribution, the neuron was considered to decrease or increase its activity during movements, respectively (Figures 4F, 4K, S4A, S4B, S4D, and S4F). The same analyses were performed to determine whether the activity was significantly changed by pharmacological manipulation of cholinergic signaling in the right M1 (Figures 7F, 7K, 7P, 7U, 8E, 8J, S8A, S8C, S8E, and S8G).

<u>Classification of movement-modulated neurons:</u> At each learning stage, movement-modulated neurons were identified by comparing the activity during the baseline period and the activity at each frame after the movement onset by bootstrap (1,000 times). The frame was classified as movement-modulated (activated or suppressed) if its p-value was less than 0.05 (two-tailed). For a given neuron, if more than 25% of the frames after movement onset were either activated or suppressed, this neuron was classified as movement-activated or movement-suppressed, respectively (Figures S4C, S4F, S8B, S8D, S8F, and S8H).

Ca event detection in cholinergic activity—The f/f trace was first smoothed (loess, 3 s) and the first derivative (velocity) of the smoothed f/f trace was calculated. The inactive portion was defined as the periods when the velocity was within the standard deviation of the whole velocity trace. Events were defined if the velocity trace crossed the standard deviation of the inactive portion of the velocity trace. This method detected sharp rises in f/f. Events with an active period less than 167 ms were excluded from further analyses. For each event, the onset time was estimated as the time when the velocity exceeded the velocity criterion (Figure S7I and S7J).

Wide-field imaging analysis—Fluorescence analysis was processed as described (Makino et al., 2017). Briefly, images were first downsampled from 512×512 to 128×128 pixels. To obtain f/f time series for each pixel, time-varying baseline fluorescence (f) was estimated for a given time point as the 10th percentile value over 30 s around it. For the beginning and end of each imaging block, the following and preceding 15 s window was used to determine the baseline, respectively. Images across sessions from the same animals were aligned to the first session using a semi-automated method written in MATLAB. To remove hemodynamic contamination and motion artifacts, f/f time series for each pixel during the peri-movement epoch (−0.5 s to 2 s relative to the movement onset) were concatenated across all trials from all sessions for each animal to perform principal component analysis followed by independent component analysis (PCA-ICA) with 80 components retained ($94.71\% \pm 0.44\%$ of the total variance, mean ± SEM). The ICA algorithm adopted in the current study was JADER (Cardoso, 1999). Independent components corresponding to hemodynamic signals and motion artifacts were visually identified and excluded (Figure S2C), and f/f time series were reconstructed using the remaining components. ROI masks of cortical regions were determined by overlaying the scaled common cortical modules on the average image from the first session in each animal (Figure S2A). Common cortical modules were previously identified based on the cortex-wide activity of excitatory neurons (Makino et al., 2017). The coordinates forthe centers of these 16 modules are (in mm): M2: ± 1.2 ML, +2.3 AP; left and right S1/M1FL: ± 3.2 ML, +1.3 AP; left and right aS1BC: ± 3.8 ML, −0.4 AP; left and right M1: ± 2.6 ML, −0.4 AP;

left and right S1HL: ± 1.8 ML, −1.0 AP; left and right pS1BC: ± 3.3 ML, −1.6 AP; PPC: ± 2.1 ML, −1.8 AP; aRSC: ± 0.8 ML, −1.8 AP; pRSC: ± 0.9 ML, −3.1 AP; left and right visual cortex: ± 3.0 ML, −3.3 AP. Pixels overlapping with main blood vessels or included in more than one module were excluded from ROI masks. For each cortical region, f/f time series was computed as the mean of the pixel values within its ROI mask. For the activity during movement epochs, the averaged activity between −367 ms and −233 ms relative to the movement onset (baseline) was subtracted from each trial, then the mean activity from 0 s to 2 s after movement onset in each trial was used for comparison between stages (Figure 2C). The activity amplitude and duration of each cortical region were analyzed using the activity from 0 s to 2 s after movement onset after subtracting the baseline period in each trial. The amplitude was measured by the maximum f/f value (peak) in each trial and the mean of all peak values was taken at each learning stage within each animal. The duration was measured by the full width at half maximum (FWHM) in each trial and the median of all FWHM values was taken at each learning stage within each animal. In a small fraction of trials (3.45% ± 0.47%, 3.23% ± 0.45%, 3.45% ± 0.47% for VIP-, SOM- and PV-INs, n (VIP) = 11 mice, n (SOM) = 12 mice, n (PV) = 11 mice, mean ± SEM), the activity did not return to half maximum within 2 s after movement onset, and in these cases the duration was defined as the interval between the time that the value went above half maximum to 2 s after movement onset.

GFP control experiments for wide-field signals—To confirm that the signals detected with our approach were calcium signals from GCaMP6f rather than artifacts, we performed control experiments using transgenic mice with GFP expressed in VIP-INs and imaging during the lever-press task (Figures S2C–S2F). We chose VIP-INs as they are the least abundant among the three IN subtypes and therefore likely to be most susceptible to artifacts with wide-field calcium imaging. The experiments and data analysis were identical to GCaMP6f-expressing animals. The wide-field signals from both GFP- and GCaMP6f-expressing mice were passed to PCA-ICA analysis to exclude hemodynamic components and then reconstructed. Using reconstructed signals, we first calculated the mean fluorescence changes (f/f) from 0 s to 2 s after movement onset of each cortical region in both groups, after subtracting the baseline period. Then, the values across cortical regions were averaged for each mouse to generate a single value for the dorsal cortex, which was further normalized to the mean value across GCaMP6f-expressing mice. For the 3 GFP-expressing mice, the relative fluorescence changes were −0.15%, 1.56%, and 5.55%, respectively (mean ± SD: 2.32% ± 2.92%). Given the heterogeneity across cortical regions, we also compared individual cortical regions between GFP- and GCaMP6f-expression mice separately, using the mean fluorescence changes during movements calculated as mentioned above. For each cortical region, the values were first averaged across GFP-expressing mice, and then normalized to the mean value across GCaMP6f-expressing mice. Using this comparison method, the relative fluorescence changes of individual cortical regions ranged 1.37% ± 6.23% (mean ± SD, M2: −1.91%, I-M1/S1FL: 10.10%, r-M1/S1FL: −5.09%, I-M1: 6.52%, r-M1: 6.82%, I-aS1BC: 1.61%, r-aS1BC: −10.16%, I-S1HL: 6.33%, r-S1HL: 10.24%, PPC: 2.08%, I-pS1BC: −2.97%, r-pS1BC: −8.24%, aRSC: 5.24%, pRSC: 1.65%, I-Visual: 3.74%, r-Visual: 4.07%). These results demonstrate that the large majority of fluorescence changes we report are indeed calcium signals.

Generalized linear model—To estimate the contributions of different behavioral events to neural activity, we constructed a generalized linear model (Musall et al., 2019; Pinto and Dan, 2015) to predict the activity of each inhibitory neuron subtype in 16 cortical regions using a set of behavioral variables as predictors. All behavioral variables were downsampled to 30 Hz to match the imaging frame rate. The predictors included both analog and binary predictors related to lever-press movements, licking, auditory cue, and reward. Predictors of each binarized behavioral variable consisted of a binary event trace containing pulses at the occurrences of the relevant event, and its time-shifted copies, each shifted in time by one frame relative to the original binary trace. For binary motor events, including the onsets of lever-press movements and licking bouts, the time-shifted copies spanned the frames from −0.5 s to +2 s relative to each event. For sensory stimuli, including the auditory cue and reward delivery sound, the time-shifted copies spanned all frames from stimulus onset until 0.5 s after each event. Analog behavioral variables, including the lever speed and licking rate, were not time-shifted. The full model had a total of 186 predictors and the general bias term. We used ridge regression (Karabatsos, 2018; Musall et al., 2019) to prevent overfitting and assessed the model performance using tenfold cross-validated correlations between the predicted and true imaged activity. The contributions of each behavioral event were assessed by calculating the predicted activity during movements as mentioned in the previous section using individual behavioral events and their coefficients in full models, and comparing the predicted activity with the true activity (Figure 3).

Pupillometry recordings—The right eye was monitored using a commercial camera (DMK 23U618, The Imaging Source) mounted with a CCTV lens (35mm f/1.7, Fujian) through 4-5 extension rings (5mm, RioRand). Images were acquired using IC Capture 2.4 (The Imaging Source) at 15 Hz, 640×480 pixels. The light source for the camera was an IR LED illuminator (IRINB04L, JCHENG). Frame times were recorded and synchronized with behavioral recordings by the Ephus software. To prevent complete pupil dilation in darkness, a blue led array lamp (LIU470A, Thorlabs) softened with several layers of Kimwipes paper (Kimberly-Clark Professional) was placed ~60 cm away in front of animals to provide ambient light in the task. The space between the craniotomy window and the microscope objective was enclosed with a blackout material (Thorlabs) to protect calcium imaging from contamination from the IR and ambient light. After the end of each session, the blue led array lamp was blocked with a black cap, and the fully dilated pupil in darkness was imaged for ~30 s as the baseline.

The pupil diameter was fitted off-line with custom codes written in MATLAB. Before fitting images from the entire session, every 100th frame was collected and parameters for pupil fitting were manually tuned on this subset. Each frame was denoised with 2D-meidan filtering (3×3 neighborhood around) and segmented using Otsu's multilevel threshold method. The darkest cluster containing more than 5000 pixels was used to generate a binary image for further refinement. The hole corresponding to the corneal reflection of the IR illuminator was filled first, and then the largest connected region in the binary image was retained as the mask for pupil edge detection. Edges were detected using Canny method. The pupil center was roughly estimated using the mean coordinates of the mask. Edges corresponding to the eyelids and small reflection spots were eliminated based on

the distance and angle relative to the pupil center. The remaining edges were visually inspected, and those not aligned with the true pupil boundary were cropped out by ROIs drawn manually. The cleaned edges were fitted with an ellipse with Hough transform and the length of the long axis of the ellipse was taken as pupil diameter (Figure S6A). The parameters tuned on this subset of frames, including the number of pixel clusters, ROIs, and fitting parameters in Hough transform, were used to fit the entire session. For baseline recording, parameters were directly tuned on the entire image set (~450 frames for 30 s). ~40 images with good fitting were manually selected, and their averaged pupil diameter was used as baseline diameter. Pupil diameter during task performance was normalized to the baseline diameter within each session to control for individual variances in pupil size and distance to the camera. For pupil diameter during the peri-movement epoch, the averaged pupil diameter between −500 ms and 0 ms relative to movement onset at the naive stage was subtracted to control for the individual variances in the sensitivity to the ambient light (Figure S6B).

Optogenetic inactivation of cholinergic projections to the cortex with eOPN3
—Optogenctic inactivation was performed seven weeks after injections throughout training. The position of the laser (GL532T3, Shanghai Laser & Optics Century) was adjusted to ensure the green light covered the entire dorsal skull. In every session, the green light (~532 nm) was delivered through the skull to the entire dorsal cortex. Given that the activity already partially recovered during 10-12 min post light delivery (Figures S7I and S7J), the green light was delivered for 15 s every 5 min spanning the entire training session to achieve a continuous inactivation. The skull transmission was measured by placing moisturized fresh skull samples between the light source and power meter. The measured skull transmission was ~50%−55%. Therefore, to achieve a light intensity of ~2 mW/mm^2 at the brain surface, we adjusted the light intensity to ~4 mW/mm^2 at the skull surface.

Pharmacological manipulation of cholinergic inputs in the right M1—Imaging fields of view were first determined under the two-photon microscope before AChR drug injections. Animals were then placed under light anesthesia with 0.5%-0.8% isoflurane, and a small craniotomy was opened ~1mm away from the center of the predetermined field of view. This was to avoid heating the field of view during drilling through the glass window. We usually drilled along the window edge to avoid window cracks. Solutions of AChR drugs were injected with a beveled pipette (~20 μm tip in diameter) through the small craniotomy at the depths of 250 μm and 500 μm. Drugs were fully dissolved in saline, and ~250 nL drug solutions were injected over 5-8 min at each depth. For naive animals, a mixture of mecamylamine (3 mM, Tocris) and atropine (100 μM, Sigma-Aldrich) was injected in one of the first two sessions. The session without injections served as controls. For expert animals, a mixture of nicotine (3 μM, Sigma-Aldrich) and carbamoylcholine chloride (0.5 mM, Sigma-Aldrich) was injected in session 20, and session 19 was used as controls. Pipettes were left in the brain for ~5 min after each injection. The small craniotomy was sealed with Vetbond and cyanoacrylate glue. Following injections, animals recovered in their home cage for 40-60 min before behavioral testing and imaging.

For enhancing cholinergic signaling in naive animals, a mixture of nicotine (3 μM, Sigma-Aldrich) and carbamoylcholine chloride (0.5 mM, Sigma-Aldrich) was injected bilaterally in M1 (0.3 mm anterior and 1.5 mm lateral from the bregma) in the first two training sessions. Drug solutions were injected through small craniotomies at the depths of 250 μm and 500 μm with ~250 nL at each depth. The small craniotomy was sealed with Vetbond and cyanoacrylate glue after injections.

Immunohistochemistry—Mice were anesthetized (ketamine/xylazine, 150 mg/kg, 12 mg/kg body weight) and perfused transcardially with 4% paraformaldehyde. Brains were then cryoprotected in a 30% sucrose solution until brains sank. 50-60 mm coronal sections were cut with a microtome (Microm HM 430, Thermo Scientific) and blocked in a solution consisting of 10% donkey serum, 1% BSA, and 0.3% Triton X-100 in 1 × PBS for 1 h at room temperature. They were then incubated overnight at 4°C with primary antibodies (1:1000 Chicken anti-GFP, Aves Labs; 1:300 Goat anti-ChAT, Millipore; Rabbit anti-mCherry, Abcam) diluted in the blocking solution. After washing, sections were incubated in Alexa Fluor-conjugated secondary antibodies (1:1000 anti-chicken 488, Jackson Immuno Research; 1:1000 anti-goat 594, Jackson Immuno Research ; 1:1000 anti-rabbit 594, Invitrogen) for 2 h at room temperature. Slices were mounted with a CC mounting medium (Sigma-Aldrich) and imaged using a fluorescence microscope (Zen and ApoTome.2, Zeiss).

QUANTIFICATION AND STATISTICAL ANALYSIS

Experimenters were not blind to the experimental conditions. Statistical significance was defined by alpha pre-set to 0.05. Error bars indicate standard errors of the mean (SEM) unless noted otherwise. All the statistical details are described in the figure legends and each test was selected based on data distributions using histograms. Sample sizes were predetermined without any statistical methods but based on those generally employed in the field. Two-tailed tests were used unless noted otherwise. Multiple comparisons were corrected by false discovery rate. Formulas used in the mixed-effects model are listed below.

For the behavior performance throughout training (Figures 1B, 1E, S1A–S1C):

$$y \sim 1 + session + (1 \mid animal) + (session - 1 \mid animal)$$

where $(1 \mid animal)$ and $(session - 1 \mid animal)$ indicate a random effect constant and a random effect slope term for each animal, $session$ is a discrete variable representing the training session, $animal$ is a categorical variable representing the animal identity, and y is behavioral measurement. The coefficient of $session$ was tested against 0.

For the comparison of activity and pupil diameter during movements throughout learning (Figures 2C, 4D, 4E, 4I, 4J, 6C, and S6B):

$$y \sim 1 + stage + (1 \mid animal) + (stage - 1 \mid aniaml)$$

where (1|*animal*) and (*stage* − 1|*aniamal*) indicate a random effect constant and a random effect slope term for each animal, *stage* is a discrete variable representing the learning stage, and *y* is the activity or pupil diameter during movements. The coefficient of *stage* was tested against 0.

For the comparison of activity during movements between the hM4Di and mCherry groups (Figures 5D and 5E):

$$y \sim 1 + group + (1 \mid animal)$$

where (1|*animal*) indicates a random effect constant, *group* is a categorical variable indicating which group the animal belonged to, and *y* is the activity during movements. The coefficient of *group* was tested against 0.

For the comparison of behavior performance between the hM4Di and mCherry groups (Figures 5F, 5G, and S5D), or between the ablation and control groups (Figures 6E, 6F, and S7G), or between the eOPN3 and mCherry groups (Figures 6H, 6I, and S7K), or between the agonist and saline groups in naive mice (Figure 6J):

$$y \sim 1 + group + (1 \mid session)$$

where (1|*session*) indicates a random effect constant, *group* is a categorical variable indicating which group the animal belonged to, and *y* is behavioral measurement. The coefficient of *group* was tested against 0.

For the comparison of activity during movements and behavior performance between pharmacological manipulation and control sessions (Figures 7D, 7E, 7I, 7J, 7N, 7O, 7S, 7T, 8C, 8D, 8H, 8I, S8I, and S8J):

$$y \sim 1 + drug + (1 \mid animal) + (drug - 1 \mid animal)$$

where (1|*animal)* and (*drug* − 1|*aniamal*) indicate a random effect constant and a random effect slope term for each animal, *drug* is a categorical variable indicating whether the session was the manipulation or control session, and *y* is the activity during movements or behavioral measurement. The coefficient of *drug* was tested against 0.

Supplementary Material

Refer to Web version on PubMed Central for supplementary material.

Acknowledgments

References

Adler A, Zhao R, Shin ME, Yasuda R, and Gan WB (2019). Somatostatin-expressing interneurons enable and maintain learning-dependent sequential activation of pyramidal neurons. Neuron 102, 202–216.e7 doi: 10.1016/j.neuron.2019.01.036. [PubMed: 30792151]

Ährlund-Richter S, Xuan Y, van Lunteren JA, Kim H, Ortiz C, Pollak Dorocic I, Meletis K, and Carlén M (2019). A whole-brain atlas of monosynaptic input targeting four different cell types in the medial prefrontal cortex of the mouse. Nat. Neurosci 22, 657–668 doi: 10.1038/s41593-019-0354-y. [PubMed: 30886408]

Allen NJ, and Eroglu C (2017). Cell biology of astrocyte-synapse interactions. Neuron 96, 697–708 doi: 10.1016/j.neuron.2017.09.056. [PubMed: 29096081]

Arriaga M, and Han EB (2019). Structured inhibitory activity dynamics in new virtual environments. Elife 8, e47611 doi: 10.7554/eLife.47611. [PubMed: 31591960]

Arroyo S, Bennett C, Aziz D, Brown SP, and Hestrin S (2012). Prolonged disynaptic inhibition in the cortex mediated by slow, non-α7 nicotinic excitation of a specific subset of cortical interneurons. J. Neurosci 32, 3859–3864 doi: 10.1523/JNEUROSCI.0115-12.2012. [PubMed: 22423106]

Ballinger EC, Ananth M, Talmage DA, and Role LW (2016). Basal forebrain cholinergic circuits and signaling in cognition and cognitive decline. Neuron 91, 1199–1218 doi: 10.1016/j.neuron.2016.09.006. [PubMed: 27657448]

Bicks LK, Yamamuro K, Flanigan ME, Kim JM, Kato D, Lucas EK, Koike H, Peng MS, Brady DM, Chandrasekaran S, et al. (2020). Prefrontal parvalbumin interneurons require juvenile social experience to establish adult social behavior. Nat. Commun 11, 1003 doi: 10.1038/s41467-020-14740-z. [PubMed: 32081848]

Bloodgood BL, Sharma N, Browne HA, Trepman AZ, and Greenberg ME (2013). The activity-dependent transcription factor NPAS4 regulates domain-specific inhibition. Nature 503, 121–125 doi: 10.1038/nature12743. [PubMed: 24201284]

Broussard GJ, Liang Y, Fridman M, Unger EK, Meng G, Xiao X, Ji N, Petreanu L, and Tian L (2018). In vivo measurement of afferent activity with axon-specific calcium imaging. Nat. Neurosci 21, 1272–1280 doi: 10.1038/s41593-018-0211-4. [PubMed: 30127424]

Cardoso JF (1999). High-order contrasts for independent component analysis. Neural Comput. 11, 157–192 doi: 10.1162/089976699300016863. [PubMed: 9950728]

Chen N, Sugihara H, and Sur M (2015a). An acetylcholine-activated microcircuit drives temporal dynamics of cortical activity. Nat. Neurosci 18, 892–902 doi: 10.1038/nn.4002. [PubMed: 25915477]

Chen SX, Kim AN, Peters AJ, and Komiyama T (2015b). Subtype-specific plasticity of inhibitory circuits in motor cortex during motor learning. Nat. Neurosci 18, 1109–1115 doi: 10.1038/nn.4049. [PubMed: 26098758]

Chen T-W, Wardill TJ, Sun Y, Pulver SR, Renninger SL, Baohan A, Schreiter ER, Kerr R. a, Orger MB, Jayaraman V, et al. (2013). Ultrasensitive fluorescent proteins for imaging neuronal activity. Nature 499, 295–300 doi: 10.1038/nature12354. [PubMed: 23868258]

Cichon J, and Gan W-B (2015). Branch-specific dendritic Ca^{2+} spikes cause persistent synaptic plasticity. Nature 520, 180–185 doi: 10.1038/naturel4251. [PubMed: 25822789]

Colangelo C, Shichkova P, Keller D, Markram H, and Ramaswamy S (2019). Cellular, synaptic and network effects of acetylcholine in the neocortex. Front. Neural Circuits 13, 24 doi: 10.3389/fncir.2019.00024. [PubMed: 31031601]

Crouse RB, Kim K, Batchelor HM, Girardi EM, Kamaletdinova R, Chan J, Rajebhosale P, Pittenger ST, Role LW, Talmage DA, et al. (2020). Acetylcholine is released in the basolateral amygdala in response to predictors of reward and enhances the learning of cue-reward contingency. Elife 9, e57335 doi: 10.7554/eLife.57335. [PubMed: 32945260]

Dasgupta R, Seibt F, and Beierlein M (2018). Synaptic release of acetylcholine rapidly suppresses cortical activity by recruiting muscarinic receptors in layer 4. J. Neurosci 38, 5338–5350 doi:10.1523/JNEUROSCI.0566-18.2018. [PubMed: 29739869]

Do JP, Xu M, Lee SH, Chang WC, Zhang S, Chung S, Yung TJ, Fan JL, Miyamichi K, Luo L, et al. (2016). Cell type-specific long-range connections of basal forebrain circuit. Elife 5, e13214 doi: 10.7554/eLife.13214. [PubMed: 27642784]

Donato F, Rompani SB, and Caroni P (2013). Parvalbumin-expressing basket-cell network plasticity induced by experience regulates adult learning. Nature 504, 272–276 doi: 10.1038/nature12866. [PubMed: 24336286]

Fu Y, Tucciarone JM, Espinosa JS, Sheng N, Darcy DP, Nicoll RA, Huang ZJ, and Stryker MP (2014). A cortical circuit for gain control by behavioral state. Cell 156, 1139–1152 doi: 10.1016/j.cellL.2014.01.050. [PubMed: 24630718]

Fu Y, Kaneko M, Tang Y, Alvarez-Buylla A, and Stryker MP (2015). A cortical disinhibitory circuit for enhancing adult plasticity. Elife 4, e05558 doi: 10.7554/eLife.05558. [PubMed: 25626167]

Gasselin C, Hohl B, Vernet A, Crochet S, and Petersen CCH (2021). Cell-type-specific nicotinic input disinhibits mouse barrel cortex during active sensing. Neuron 109, 778–787.e3. doi: 10.1016/j.neuron.2020.12.018. [PubMed: 33472037]

Guo W, Robert B, and Polley DB (2019). The cholinergic basal forebrain links auditory stimuli with delayed reinforcement to support learning. Neuron 103, 1164–1177.e6 doi:10.1016/j.neuron.2019.06.024. [PubMed: 31351757]

Hangya B, Ranade SP, Lorenc M, and Kepecs A (2015). Central cholinergic neurons are rapidly recruited by reinforcement feedback. Cell 162, 1155–1168 doi: 10.1016/j.cell.2015.07.057. [PubMed: 26317475]

Hasselmo ME, and Sarter M (2011). Modes and models of forebrain cholinergic neuromodulation of cognition. Neuropsychopharmacology 36, 52–73 doi: 10.1038/npp.2010.104. [PubMed: 20668433]

Hattori R, and Komiyama T (2021). PatchWarp: Corrections of non-uniform image distortions in two-photon calcium imaging data by patchwork affine transformations. bioRxiv 468164 doi: 10.1101/2021.11.10.468164. Date: 2021.11.13

Hattori R, Kuchibhotla KV, Froemke RC, and Komiyama T (2017). Functions and dysfunctions of neocortical inhibitory neuron subtypes. Nat. Neurosci 20, 1199–1208 doi: 10.1038/nn.4619. [PubMed: 28849791]

He M, Tucciarone J, Lee S, Osten P, Rudy B, Huang Correspondence J, Nigro MJ, Kim Y, Levine JM, Kelly SM, et al. (2016). Strategies and tools for combinatorial targeting of GABAergic neurons in mouse cerebral cortex. Neuron 91, 1–16 doi: 10.1016/j.neuron.2016.08.021. [PubMed: 27387643]

Hippenmeyer S, Vrieseling E, Sigrist M, Portmann T, Laengle C, Ladle DR, and Arber S (2005). A developmental switch in the response of DRG neurons to ETS transcription factor signaling. PLoS Biol. 3, 0878–0890 doi: 10.1371/journal.pbio.0030159.

Jaffe PI, and Brainard MS (2020). Acetylcholine acts on songbird premotor circuitry to invigorate vocal output. Elife 9, e53288 doi: 10.7554/eLife.53288. [PubMed: 32425158]

Jiang X, Shen S, Cadwell CR, Berens P, Sinz F, Ecker AS, Patel S, and Tolias AS (2015). Principles of connectivity among morphologically defined cell types in adult neocortex. Science 350, aac9462 doi: 10.1126/science.aac9462. [PubMed: 26612957]

Karabatsos G (2018). Marginal maximum likelihood estimation methods for the tuning parameters of ridge, power ridge, and generalized ridge regression. Commun. Stat. Simul. Comput 47, 1632–1651 doi: 10.1080/03610918.2017.1321119.

Karnani MMM, Jackson J, Ayzenshtat I, Tucciarone J, Manoocheri K, Snider WGG, and Yuste R (2016). Cooperative subnetworks of molecularly similar interneurons in mouse neocortex. Neuron 90, 86–100 doi: 10.1016/j.neuron.2016.02.037. [PubMed: 27021171]

Kepecs A, and Fishell G (2014). Interneuron cell types are fit to function. Nature 505, 318–326 doi: 10.1038/nature12983. [PubMed: 24429630]

Kim D, Jeong H, Lee J, Ghim JW, Her ES, Lee SH, and Jung MW (2016a). Distinct roles of parvalbumin- and somatostatin-expressing interneurons in working memory. Neuron 92, 902–915 doi: 10.1016/j.neuron.2016.09.023. [PubMed: 27746132]

Kim J, Jung A, Jeong D, Choi I, Kim K, Shin S, Kim SJ, and Lee XS (2016b). Selectivity of neuromodulatory projections from the basal forebrain and locus ceruleus to primary

Author Manuscript

sensory cortices. J. Neurosci 36, 5314–5327 doi: 10.1523/JNEUROSCI.4333-15.2016. [PubMed: 27170128]

Kim TH, Zhang Y, Lecoq J, Jung JC, Li J, Zeng H, Niell CM, and Schnitzer MJ (2016c). Long-term optical access to an estimated one million neurons in the live mouse cortex. Cell Rep. 17, 3385–3394 doi: 10.1016/j.celrep.2016.12.004. [PubMed: 28009304]

Komiyama T, Sato TR, O'Connor DH, Zhang Y-X, Huber D, Hooks BM, Gabitto M, and Svoboda K (2010). Learning-related fine-scale specificity imaged in motor cortex circuits of behaving mice. Nature 464, 1182–1186 doi: 10.1038/nature08897. [PubMed: 20376005]

Krabbe S, Paradiso E, Aquin S, Bitterman Y, Courtin J, Xu C, Yonehara K, Markovic M, Müller C, Eichlisberger T, et al. (2019). Adaptive disinhibitory gating by VIP interneurons permits permits associative learning. Nat. Neurosci 22, 1834–1843 doi: 10.1038/s41593-019-0508-y. [PubMed: 31636447]

Krashes MJ, Koda S, Ye CP, Rogan SC, Adams AC, Cusher DS, Maratos-Flier E, Roth BL, and Lowell BB (2011). Rapid, reversible activation of AgRP neurons drives feeding behavior in mice. J. Clin. Inves 121, 1424–1428 doi: 10.1172/JCI46229.

Kruglikov I, and Rudy B (2008). Perisomatic GABA release and thalamocortical integration onto neocortical excitatory cells are regulated by neuromodulators. Neuron 58, 911–924 doi: 10.1016/j.neuron.2008.04.024. [PubMed: 18579081]

Kuchibhotla KV, Gill JV, Lindsay GW, Papadoyannis ES, Field RE, Sten TAH, Miller KD, and Froemke RC (2016). Parallel processing by cortical inhibition enables context-dependent behavior. Nat. Neurosci 20, 62–71 doi: 10.1038/nn.4436. [PubMed: 27798631]

Lee S, Kruglikov I, Huang ZJ, Fishell G, and Rudy B (2013). A disinhibitory circuit mediates motor integration in the somatosensory cortex. Nat. Neurosci 16, 1662–1670 doi: 10.1038/nn.3544. [PubMed: 24097044]

Letzkus JJ, Wolff SBE, and Lu A (2015). Disinhibition, a circuit mechanism for associative learning and memory. Neuron 88, 264–276 doi: 10.1016/j.neuron.2015.09.024. [PubMed: 26494276]

Levelt CN, and Hübener M (2012). Critical-period plasticity in the visual cortex. Annu. Rev. Neurosci 35, 309–330 doi: 10.1146/annurev-neuro-061010-113813. [PubMed: 22462544]

Li X, Yu B, Sun Q, Zhang Y, Ren M, Zhang X, Li A, Yuan J, Madisen L, Luo Q, et al. (2018). Generation of a whole-brain atlas for the cholinergic system and mesoscopic projectome analysis of basal forebrain cholinergic neurons. Proc. Natl. Acad. Sci 115, 415–420 doi: 10.1073/pnas.1703601115. [PubMed: 29259118]

Lin S-C, Brown RE, Hussain Shuler MG, Petersen CCH, and Kepecs A (2015). Optogenetic dissection of the basal forebrain neuromodulatory control of cortical activation, plasticity, and cognition. J. Neurosci 35, 13896–13903 doi: 10.1523/JNEUROSCI.2590-15.2015. [PubMed: 26468190]

Lohani S, Moberly AH, Benisty H, Landa B, Jing M, Li Y, Higley MJ, and Cardin JA (2020). Dual color mesoscopic imaging reveals spatiotemporally heterogeneous coordination of cholinergic and neocortical activity. bioRxiv 418632 doi: 10.1101/2020.12.09.418632. Date: 2021.09.21

Madisen L, Garner AR, Shimaoka D, Chuong AS, Klapoetke NC, Li L, van der Bourg A, Niino Y, Egolf L, Monetti C, et al. (2015). Transgenic mice for intersectional targeting of neural sensors and effectors with high specificity and performance. Neuron 85, 942–958 doi: 10.1016/j.neuron.2015.02.022. [PubMed: 25741722]

Mahn M, Saraf-Sinik I, Patil P, Pulin M, Bitton E, Karalis N, Bruentgens F, Palgi S, Gat A, Dine J, et al. (2021). Efficient optogenetic silencing of neurotransmitter release with a mosquito rhodopsin. Neuron 109, 1621–1635.e8 doi: 10.1016/j.neuron.2021.03.013. [PubMed: 33979634]

Makino H, and Komiyama T (2015). Learning enhances the relative impact of top-down processing in the visual cortex. Nat. Neurosci 18, 1116–1122 doi: 10.1038/nn.4061. [PubMed: 26167904]

Makino H, Ren C, Liu H, Kim AN, Kondapaneni N, Liu X, Kuzum D, and Komiyama T (2017). Transformation of cortex-wide emergent properties during motor learning. Neuron 94, 880–890.e8 doi: 10.1016/j.neuron.2017.04.015. [PubMed: 28521138]

Markram H, Toledo-Rodriguez M, Wang Y, Gupta A, Silberberg G, and Wu C (2004). Interneurons of the neocortical inhibitory system. Nat. Rev. Neurosci 5, 793–807 doi: 10.1038/nrn1519. [PubMed: 15378039]

Minces V, Pinto L, Dan Y, and Chiba AA (2017). Cholinergic shaping of neural correlations. Proc. Natl. Acad. Sci. U. S. A 114, 5725–5730 doi: 10.1073/pnas.1621493114. [PubMed: 28507133]

Mitani A, and Komiyama T (2018). Real-time processing of two-photon calcium imaging data including lateral motion artifact correction. Front. Neuroinform 12, 98 doi: 10.3389/fninf.2018.00098. [PubMed: 30618703]

Munoz W, Tremblay R, Levenstein D, and Rudy B (2017). Layer-specific modulation of neocortical dendritic inhibition during active wakefulness. Science 959, 954–959 doi: 10.1126/science.aag2599.

Musall S, Kaufman MT, Juavinett AL, Gluf S, and Churchland AK (2019). Single-trial neural dynamics are dominated by richly varied movements. Nat. Neurosci 22, 1677–1686 doi: 10.1038/s41593-019-0502-4. [PubMed: 31551604]

Naka A, and Adesnik H (2016). Inhibitory circuits in cortical layer 5. Front. Neural Circuits 10, 35 doi: 10.3389/fncir.2016.00035. [PubMed: 27199675]

Nigro MJ, Hashikawa-Yamasaki Y, and Rudy B (2018). Diversity and connectivity of layer 5 somatostatin-expressing interneurons in the mouse barrel cortex. J. Neurosci 38, 1622–1633 doi: 10.1523/JNEUROSCI.2415-17.2017. [PubMed: 29326172]

Pachitariu M, Stringer C, Dipoppa M, Schröder S, Rossi LF, Dalgleish H, Carandini M, and Harris K (2016). Suite2p: beyond 10,000 neurons with standard two-photon microscopy. bioRxiv 061507 doi: 10.1101/061507. Date: 2017..07.20

Peters AJ, Chen SX, and Komiyama T (2014). Emergence of reproducible spatiotemporal activity during motor learning. Nature 510, 263–267 doi: 10.1038/nature13235. [PubMed: 24805237]

Pfeffer CK, Xue M, Fie M, Huang ZJ, and Scanziani M (2013). Inhibition of inhibition in visual cortex: the logic of connections between molecularly distinct interneurons. Nat. Neurosci 16, 1068–1076 doi: 10.1038/nn.3446. [PubMed: 23817549]

Pi H-J, Hangya B, Kvitsiani D, Sanders JI, Huang ZJ, and Kepecs A (2013). Cortical interneurons that specialize in disinhibitory control. Nature 503, 521–524 doi: 10.1038/nature12676. [PubMed: 24097352]

Pinto L, and Dan Y (2015). Cell-Type-Specific Activity in Prefrontal Cortex during Goal-Directed Behavior. Neuron 87, 437–450 doi: 10.1016/j.neuron.2015.06.021. [PubMed: 26143660]

Ramaswamy S, Colangelo C, and Markram H (2018). Data-driven modeling of cholinergic modulation of neural microcircuits: bridging neurons, synapses and network activity. Front. Neural Circuits 12, 77 doi: 10.3389/fncir.2018.00077. [PubMed: 30356701]

Reimer J, McGinley MJ, Liu Y, Rodenkirch C, Wang Q, McCormick DA, and Tolias AS (2016). Pupil fluctuations track rapid changes in adrenergic and cholinergic activity in cortex. Nat. Commun 7, 13289 doi: 10.1038/ncommsl3289. [PubMed: 27824036]

Rossi J, Balthasar N, Olson D, Scott M, Berglund E, Lee CE, Choi MJ, Lauzon D, Lowell BB, and Elmquist JK (2011). Melanocortin-4 receptors expressed by cholinergic neurons regulate energy balance and glucose homeostasis. Cell Metab. 13, 195–204 doi: 10.1016/j.cmet.2011.01.010. [PubMed: 21284986]

Roth BL (2016). DREADDs for neuroscientists. Neuron 89, 683–694 doi: 10.1016/j.neuron.2016.01.040. [PubMed: 26889809]

Rudy B, and Munoz W (2014). Spatiotemporal specificity in cholinergic control of neocortical function. Curr. Opin. Neurobiol 26, 149–160 doi: 10.1016/j.conb.2014.02.015. [PubMed: 24637201]

Rudy B, Fishell G, Lee S, and Hjerling-Leffler J (2011). Three groups of interneurons account for nearly 100% of neocortical GABAergic neurons. Dev. Neurobiol 71, 45–61 doi: 10.1002/dneu.20853. [PubMed: 21154909]

Saunders A, Macosko EZ, Wysoker A, Goldman M, Krienen FM, de Rivera H, Bien E, Baum M, Bortolin L, Wang S, et al. (2018). Molecular diversity and specializations among the cells of the adult mouse brain. Cell 174, 1015–1030.e16 doi: 10.1016/j.cell.2018.07.028. [PubMed: 30096299]

Schindelin J, Arganda-Carreras I, Frise E, Kaynig V, Longair M, Pietzsch T, Preibisch S, Rueden C, Saalfeld S, Schmid B, et al. (2012). Fiji: An open-source platform for biological-image analysis. Nat. Methods 9, 676–682 doi: 10.1038/nmeth.2019. [PubMed: 22743772]

Sciolino NR, Mazzone CM, Plummer NW, Evsyukova I, Amin J, Smith KG, McGee CA, Fry SA, Yang CX, Powell JM, et al. (2019). A role for the locus coeruleus in the modulation of feeding. bioRxiv 881599 doi: 10.1101/2019.12.18.881599. Date: 2019.12.19

Taniguchi H, Fie M, Wu P, Kim S, Paik R, Sugino K, Kvitsani D, Fu Y, Lu J, Lin Y, et al. (2011). A resource of ere driver lines for genetic targeting of GABAergic neurons in cerebral cortex. Neuron 71, 995–1013 doi: 10.1016/j.neuron.2011.07.026. [PubMed: 21943598]

Tasic B, Yao Z, Graybuck LT, Smith KA, Nguyen TN, Bertagnolli D, Goldy J, Garren E, Economo MN, Viswanathan S, et al. (2018). Shared and distinct transcriptomic cell types across neocortical areas. Nature 563, 72–78 doi: 10.1038/s41586-018-0654-5. [PubMed: 30382198]

Tremblay R, Lee S, and Rudy B (2016). GABAergic interneurons in the neocortex: from cellular properties to circuits. Neuron 91, 260–292 doi: 10.1016/j.neuron.2016.06.033. [PubMed: 27477017]

Vallentin D, Kosche G, Lipkind D, and Long MA (2016). Inhibition protects acquired song segments during vocal learning in zebra finches. Science 351, 267–271 doi: 10.1126/science.aad3023. [PubMed: 26816377]

Wall NR, De La Parra M, Sorokin JM, Taniguchi H, Huang ZJ, and Callaway EM (2016). Brain-wide maps of synaptic input to cortical interneurons. J. Neurosci 36, 4000–4009 doi:10.1523/JNEUROSCI.3967-15.2016. [PubMed: 27053207]

Williams LE, and Holtmaat A (2019). Higher-order thalamocortical inputs gate synaptic long-term potentiation via disinhibition. Neuron 101, 91–102.e4 doi: 10.1016/j.neuron.2018.10.049. [PubMed: 30472077]

Woolf NJ (1991). Cholinergic systems in mammalian brain and spinal cord. Prog. Neurobiol 37, 475–524 doi: 10.1016/0301-0082(91)90006-M. [PubMed: 1763188]

Xu T, Yu X, Perlik AJ, Tobin WF, Zweig JA, Tennant K, Jones T, and Zuo Y (2009). Rapid formation and selective stabilization of synapses for enduring motor memories. Nature 462, 915–919 doi: 10.1038/nature08389. [PubMed: 19946267]

Xue M, Atallah BV, and Scanziani M (2014). Equalizing excitation–inhibition ratios across visual cortical neurons. Nature 511, 596–600 doi: 10.1038/nature13321. [PubMed: 25043046]

Yang CF, Chiang MC, Gray DC, Prabhakaran M, Alvarado M, Juntti SA, Unger EK, Wells JA, and Shah NM (2013). Sexually dimorphic neurons in the ventromedial hypothalamus govern mating in both sexes and aggression in males. Cell 153, 896–909 doi: 10.1016/j.cell.2013.04.017. [PubMed: 23663785]

Yao Z, Liu H, Xie F, Fischer S, Adkins RS, Aldridge AI, Ament SA, Bartlett A, Behrens MM, Van den Berge K, et al. (2021). A transcriptomic and epigenomic cell atlas of the mouse primary motor cortex. Nature 598, 103–110 doi: 10.1038/s41586-021-03500-8. [PubMed: 34616066]

Zeisel A, Hochgerner H, Lönnerberg P, Johnsson A, Memic F, van der Zwan J, Höring M, Braun E, Borm LE, La Manno G, et al. (2018). Molecular architecture of the mouse nervous system. Cell 174, 999–1014.e22 doi: 10.1016/j.cell.2018.06.021. [PubMed: 30096314]

Zhang S, Xu M, Kamigaki T, Do JPH, Chang W-C, Jenvay S, Miyamichi K, Luo L, and Dan Y (2014). Long-range and local circuits for top-down modulation of visual cortex processing. Science 345, 660–665 doi: 10.1126/science.1254126. [PubMed: 25104383]

Highlights

- Global and subtype-specific modulation of IN activity during motor learning

- VIP-INs (SOM-INs) show strong (weak) activation in the initial learning phase

- Global modulation of the cholinergic inputs across cortical regions during learning

- Perturbation of the cholinergic system alters IN activity and impairs learning
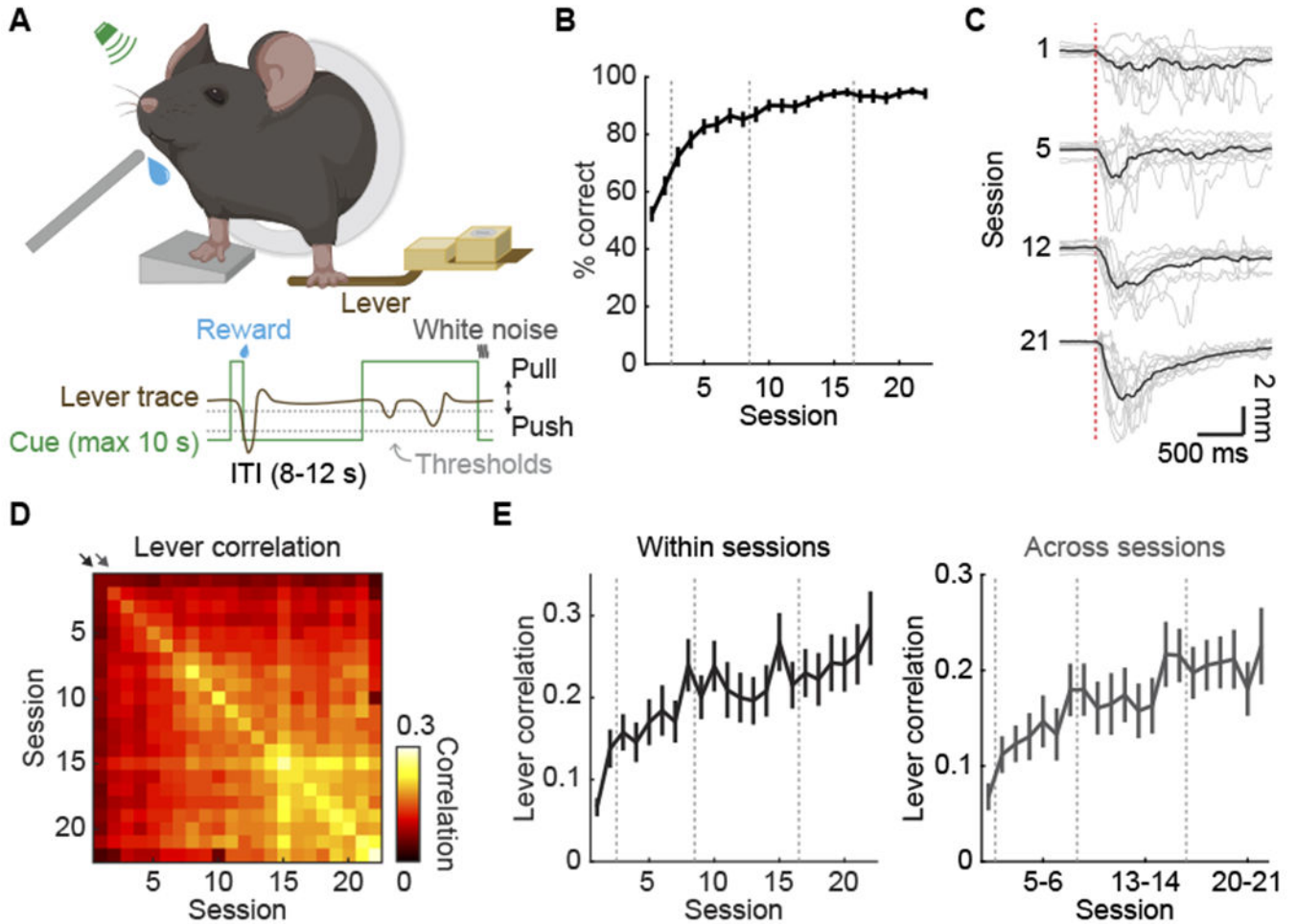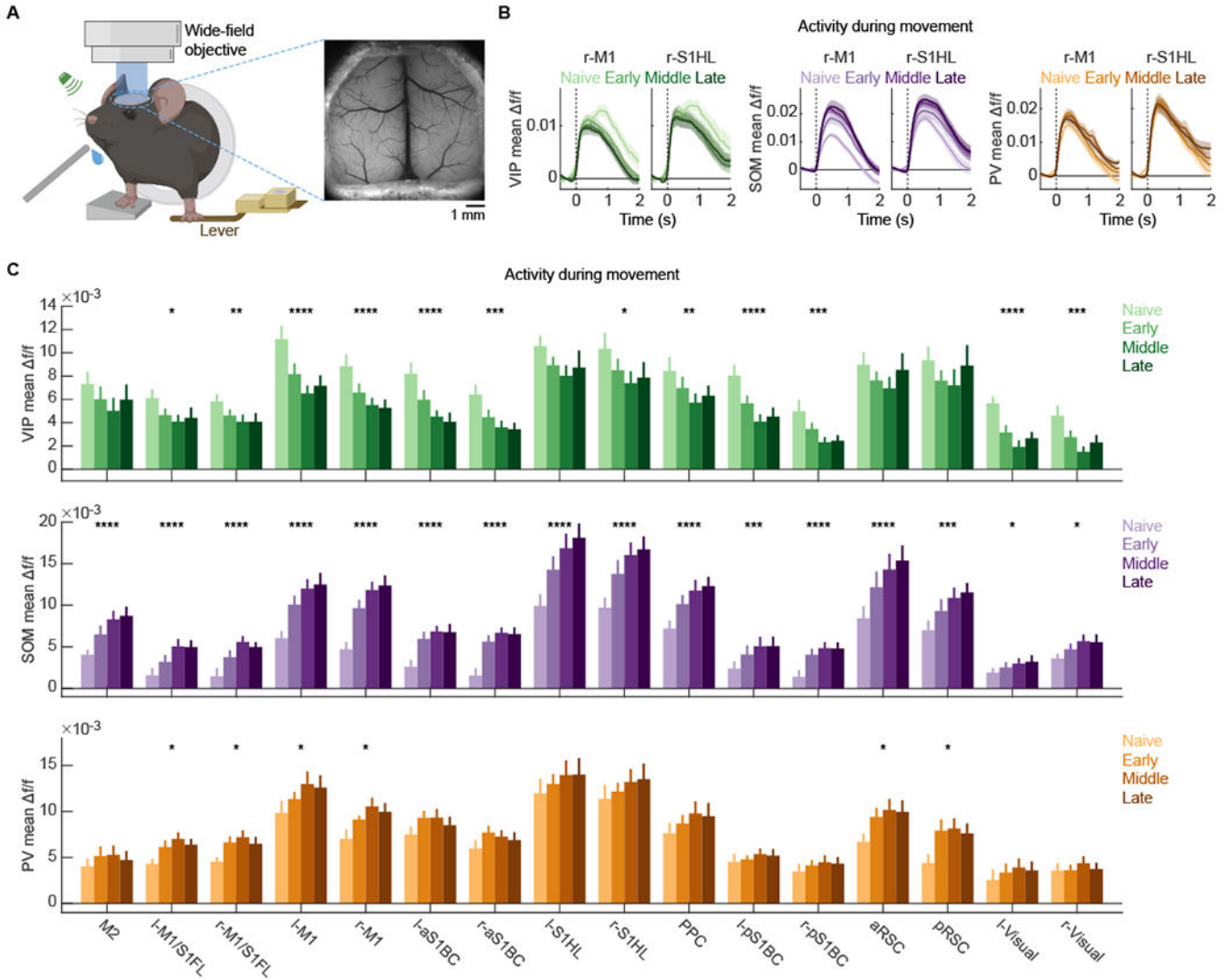
Figure 1. Motor learning task

(A) Experimental setup and task structure. ITI: inter-trial interval.

(B) Fraction of rewarded trials increases with learning (p < 0.0001, mixed-effects model, n = 40 mice from session 1 to 21, n = 17 mice for session 22, mean ± SEM). Gray dashed lines indicate the naive (session 1-2), early (session 3-8), middle (session 9-16), and late (session 17-22) stages.

(C) Example lever trajectories in rewarded trials from one mouse. Grey lines represent trajectories from randomly selected 10 trials and black lines represent their average. Red dashed line indicates the movement onset.

(D) Correlation matrix of the lever trajectories in individual trials. Each square represents the median of trial-by-trial correlation coefficients of rewarded lever-press movements within or across sessions, averaged across animals.

(E) Trial-by-trial correlations of the lever trajectories within each session and across adjacent sessions increase with training (p < 0.0001 for both comparisons, mixed-effects model, mean ± SEM). These comparisons correspond to the diagonals indicated by the black and gray arrows in (D). See also Figure S1.

Figure 2. Cortex-wide, subtype-specific modulation of IN activity during motor learning revealed by cell type-specific wide-field calcium imaging

(A) Left, experimental setup. Right: an example field of view of wide-field calcium imaging.Scale bar, 1 mm.

(B) Activity of VIP-, SOM- and PV-INs aligned to the movement onset from example cortical regions, averaged across animals (n (VIP) = 11 mice, n (SOM) = 12 mice, n (PV) = 11 mice, mean ± SEM). S1HL: primary somatosensory cortex hindlimb area.

(C) Activity of VIP-, SOM- and PV-INs during movements in individual cortical regions at each learning stage (indicated by colors), measured by mean f/f between 0 and +2 s relative to the movement onset (*$p < 0.05$, **$p < 0.01$, ***$p < 0.001$, ****$p < 0.0001$, mixed-effects model, corrected for multiple comparisons by false discovery rate, mean ± SEM). See also Figures S2, S3, and Movie S1.
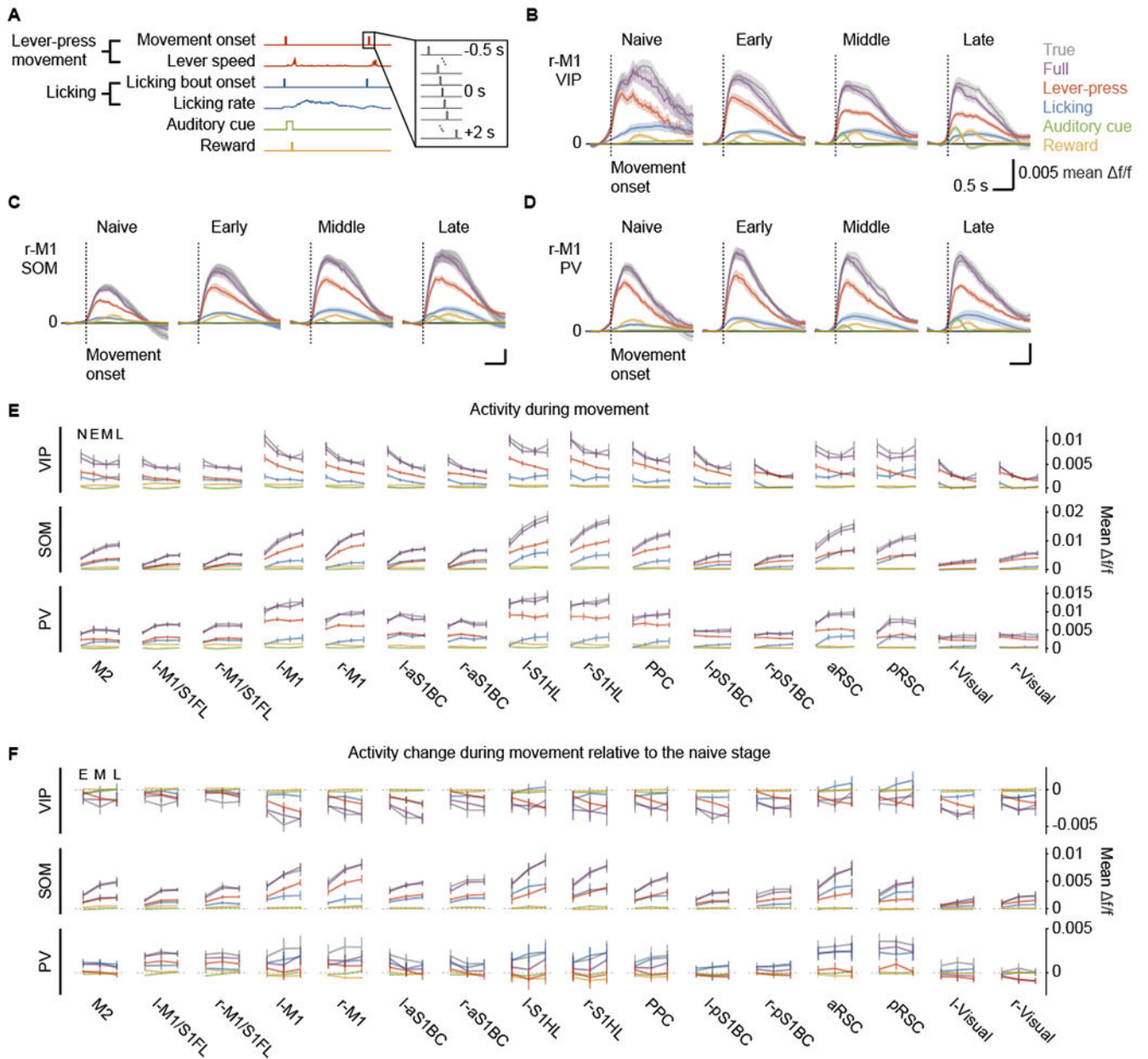
Figure 3. Contributions of various behavioral events to cortex-wide IN activity characterized by a generalized linear model

(A) Predictors in the generalized linear model. Binary behavioral events are time-shifted to account for potential lags between the events and neural activity.

(B-D) The true imaged activity and the activity predicted by the full model or individual behavioral events of each IN subtype in r-M1 as examples, aligned to the movement onset and averaged across animals (n (VIP) = 11 mice, n (SOM) = 11 mice, n (PV) = 11 mice, mean ± SEM). Note that the full model closely fit the activity profile.

(E) True or predicted activity during movements averaged across animals (mean ± SEM). N: naive, E: early, M: middle, L: late.

(F) Contributions of behavioral events to learning-related changes of cortex-wide IN activity during movements, compared to the naive stage (mean ± SEM). Color code in (C)-(F) is the same as in (B).
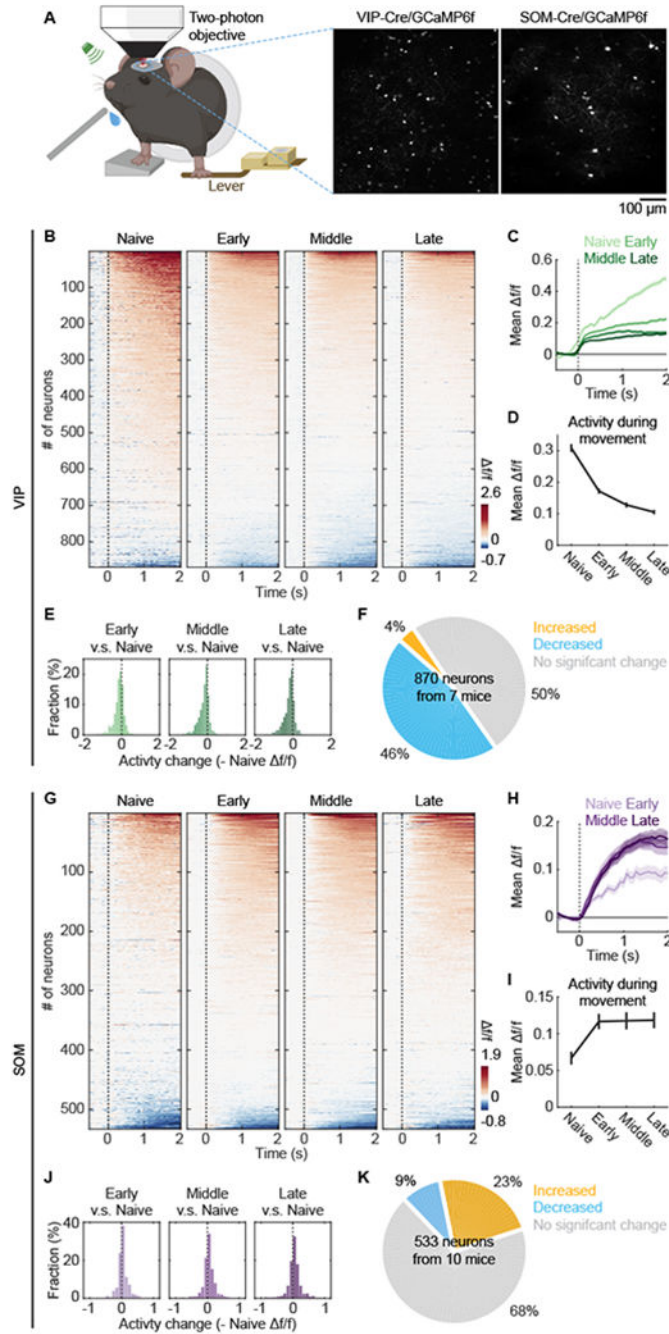
Figure 4. Subtype-specific modulation of the activity during movements of individual VIP- and SOM-INs in M1 during motor learning.

(A) Example fields of view of two-photon calcium imaging of VIP- and SOM-INs in the right M1. Scale bar, 100 μm.

(B) Activity of VIP-INs at each learning stage aligned to the movement onset (870 VIP-INs from 7 mice). Each row represents the activity averaged across trials of individual neurons, sorted according to their activity level during movements within each stage.

(C) Activity of VIP-INs averaged across movements and neurons at each learning stage aligned to the movement onset (mean ± SEM).

(D) Activity during movements averaged across VIP-INs at each learning stage (p < 0.0001, mixed-effects model, mean ± SEM).

(E) Distribution of changes in the activity level during movements across VIP-INs at the early, middle, and late stages compared to the naive stage (Early v.s. Naive: p < 0.0001, Middle v.s. Naive: p < 0.0001, Late v.s. Naive: p < 0.0001, mixed-effects model, corrected for multiple comparisons by false discovery rate).

(F) The fraction of VIP-INs with significant changes in the activity level during movements at the late stage compared to the naive stage.

(G)-(K) Same as (B)-(F) but for SOM-INs (533 SOM-INs from 10 mice). For (I), p = 0.0007, mixed-effects model. For (J), Early v.s. Naive: p = 0.0011, Middle v.s. Naive: p = 0.0011, Late v.s. Naive: p = 0.0011, mixed-effects model, corrected for multiple comparisons by false discovery rate. The activity of SOM-INs during movements is weak at the naive stage and increases with further training. See also Figure S4.
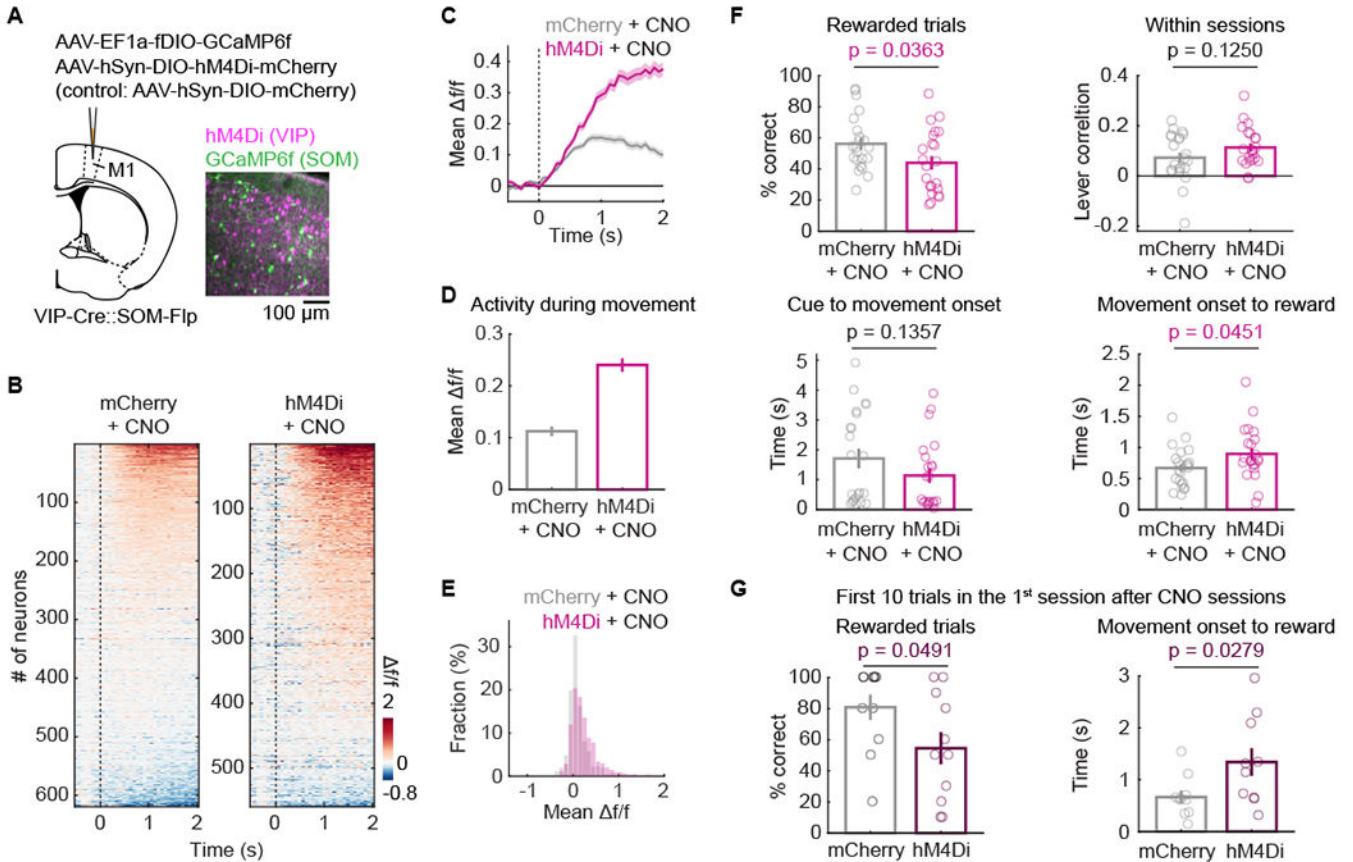
Figure 5. Inactivation of VIP-INs in naive animals increases SOM-IN activity and impairs motor learning

(A) Schematic of injections to selectively express hM4Di (or mCherry in controls) in VIP-INs and GCaMP6f in SOM-INs in the right M1. Scale bar, 100 μm.

(B) Activity of SOM-INs at the naive stage aligned to the movement onset (619 neurons from 11 animals in the mCherry group, 559 neurons from 11 animals in the hM4Di group). Each row represents the activity averaged across trials of individual neurons, sorted according to their activity level during movements.

(C) Averaged activity of SOM-INs in mCherry and hM4Di groups aligned to the movement onset (mean ± SEM).

(D) Activity during movements averaged across SOM-INs in mCherry and hM4Di groups (p = 0.0186, mixed-effects model, mean ± SEM).

(E) Distribution of the activity level of SOM-INs during movements in mCherry and hM4Di groups. Note the rightward shift of the hM4Di group compared to the mCherry group.

(F) Behavior performance of naive animals in mCherry and hM4Di groups in CNO sessions (mixed-effects model, n (hM4Di) = n (mCherry) = 11 mice, 2 sessions per animal, mean ± SEM). Circles represent behavioral measurements of individual sessions.

(G) Behavioral performance in the first 10 trials in the first session after the CNO sessions (mixed-effects model, 11 animals in each group). Circles represent behavioral measurements of individual animals. See also Figure S5.
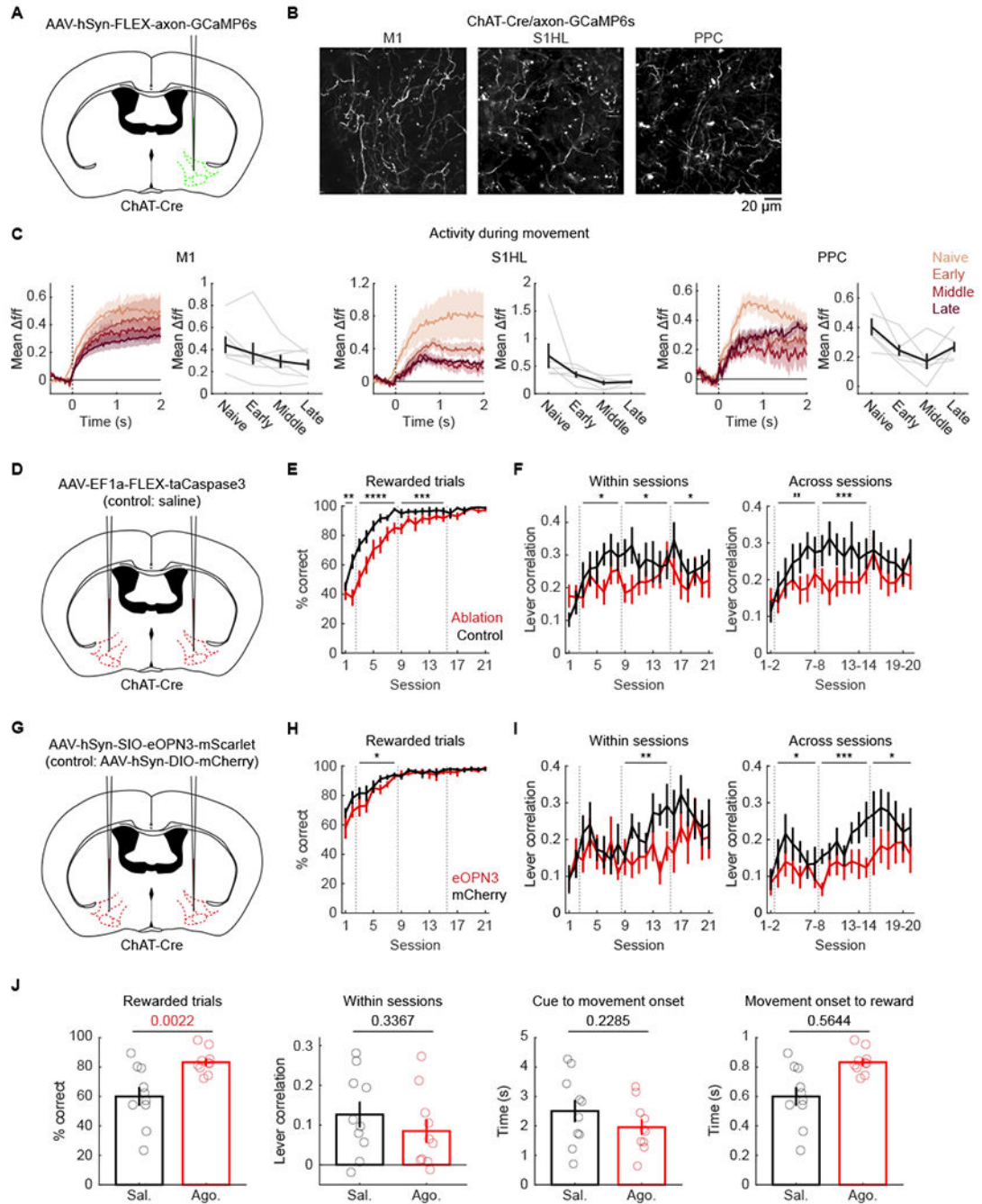
Figure 6. The basal forebrain cholinergic system is involved in motor learning

(A) Schematic of injections to selectively express axon-GCaMP6s in basal forebrain cholinergic neurons.

(B) Example fields of view of two-photon calcium imaging of basal forebrain cholinergic axons in the right M1, S1HL, and PPC. Scale bar, 20 μm.

(C) Traces show the activity of cholinergic axons at each learning stage aligned to the movement onset (n (Ml) = 7 mice, n (SIHL) = 6 mice, n (PPC) = 6 mice, mean ± SEM). Line plots show the averaged activity of cholinergic axons during movements at each

learning stage (p (M1) = 0.0016, p (S1HL) = 0.0059, p (PPC) = 0.0190, mixed-effects model, mean ± SEM). Gray lines represent individual animals.

(D) Schematic of injections to selectively ablate basal forebrain cholinergic neurons bilaterally through Caspase3 expression.

(E) Behavior performance of ablation and control groups (**p < 0.01, ***p < 0.001, ****p < 0.0001, mixed-effects model, n (Ablation) = 15 mice, n (Control) = 13 mice, mean ± SEM). Gray dashed lines indicate the naive (session 1-2), early (session 3-8), middle (session 9-16), and late (session 17-22) stages.

(F) Trial-by-trial correlations of the lever trajectories within (left) and across (right) sessions (*p < 0.05, **p < 0.01, ***p < 0.001, mixed-effects model, mean ± SEM).

(G) Schematic of injections to selectively express eOPN3 or mCherry in basal forebrain cholinergic neurons bilaterally.

(H) Behavior performance of eOPN3 and mCherry groups (*p < 0.05, mixed-effects model, n (eOPN3) = 9 mice, n (mCherry) = 8 mice, mean ± SEM).

(I) Trial-by-trial correlations of the lever trajectories within (left) and across (right) sessions (*p < 0.05, **p < 0.01, ***p < 0.001, mixed-effects model, mean ± SEM).

(J) Naive mice receiving bilateral injections of AChR agonists (3 μM nicotine and 0.5 mM carbamoylcholine chloride) into M1 showed a higher fraction of rewarded trials than mice receiving saline injections (mixed-effects model, n (Ago.) = 5 mice, n (Sal.) = 5 mice, 2 sessions per animal, mean ± SEM). Circles represent behavioral measurements of individual sessions. Sal.: saline, Ago.: agonists. See also Figures S6 and S7.
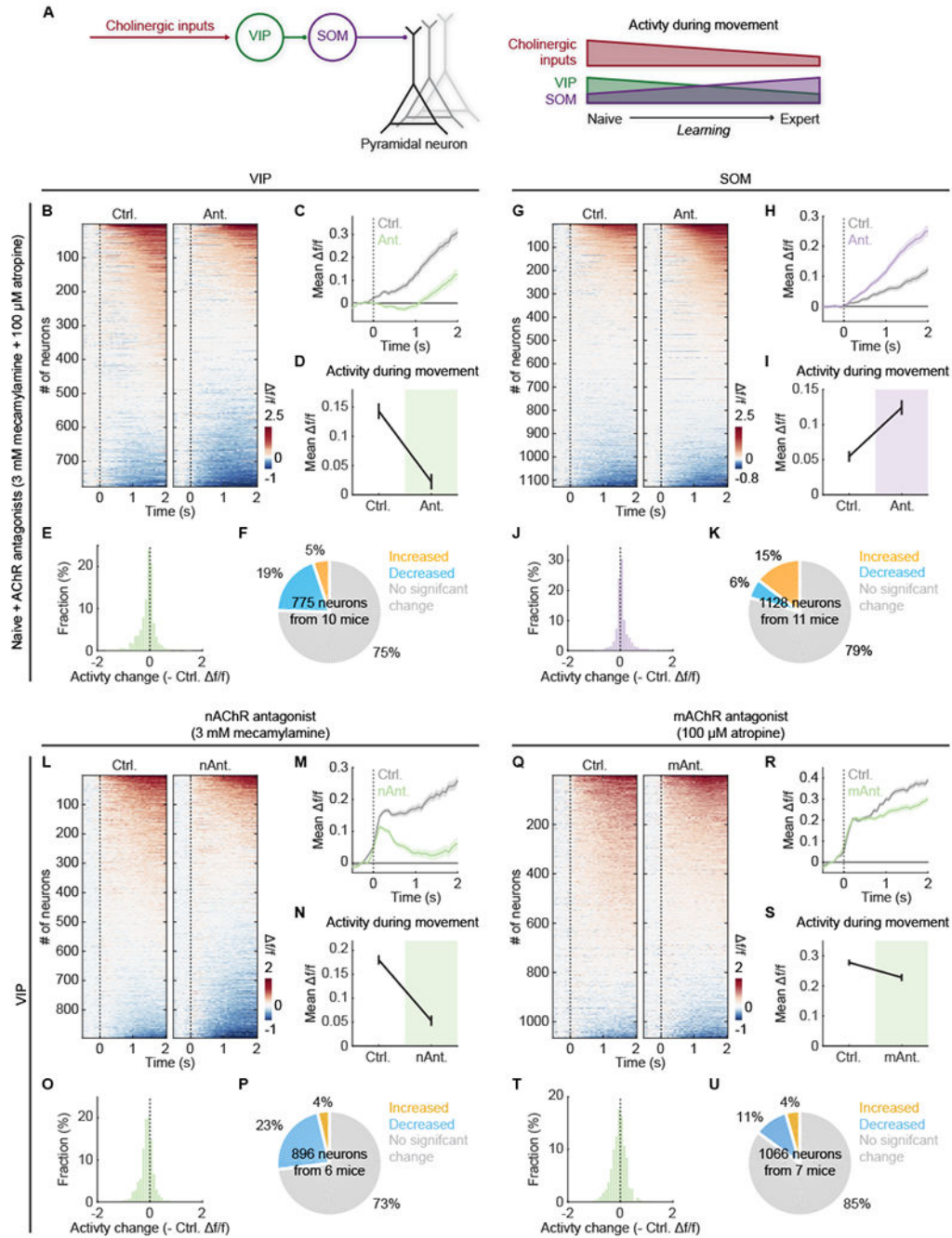
Figure 7. Pharmacological inactivation of cholinergic signaling decreases VIP- and increases SOM-IN activity during movements in naive mice

(A) Schematic of the model for learning-related modulation in cortical circuits.

(B) Activity of VIP-INs in the right M1 at the naive stage aligned to the movement onset, with or without local applications of AChR antagonists (775 VIP-INs from 10 mice). Each row represents the activity averaged across trials of individual neurons, sorted according to their activity level during movements within each session. Ctrl.: control sessions, Ant.: manipulation sessions with AChR antagonists.

(C) Activity of VIP-INs averaged across movements and neurons in control and manipulation sessions aligned to the movement onset (mean ± SEM).

(D) Activity during movements averaged across VIP-INs in control and manipulation sessions (p = 0.0024, mixed-effects model, mean ± SEM).

(E) Distribution of changes in the activity level of VIP-INs during movements in the manipulation session compared to the control session.

(F) Fraction of VIP-INs with significant changes in the activity level during movements in the manipulation session compared to the control session at the naive stage.

(G)-(K) Same as (B)-(F) but for SOM-INs (1128 SOM-INs from 11 mice). For (I), AChR antagonists increased the activity of SOM-INs during movements in naive animals, p = 0.0062, mixed-effects model, mean ± SEM.

(L)-(P) Same as (B)-(F) but in naive animals with local applications of only nAChR antagonist in the right M1 (896 VIP-INs from 6 mice). For (N), nAChR antagonist significantly reduced the activity of VIP-INs in naive animals (p = 0.0031, mixed-effects model, mean ± SEM). Ctrl.: control sessions, nAnt.: manipulation sessions with nAChR antagonist.

(Q)-(U) Same as (B)-(F) but with mAChR antagonist (1066 VIP-INs from 7 mice). For (S), mAChR antagonist did not significantly decrease the mean activity of VIP-INs in naive animals (p = 0.2302, mixed-effects model, mean ± SEM). See also Figure S8.
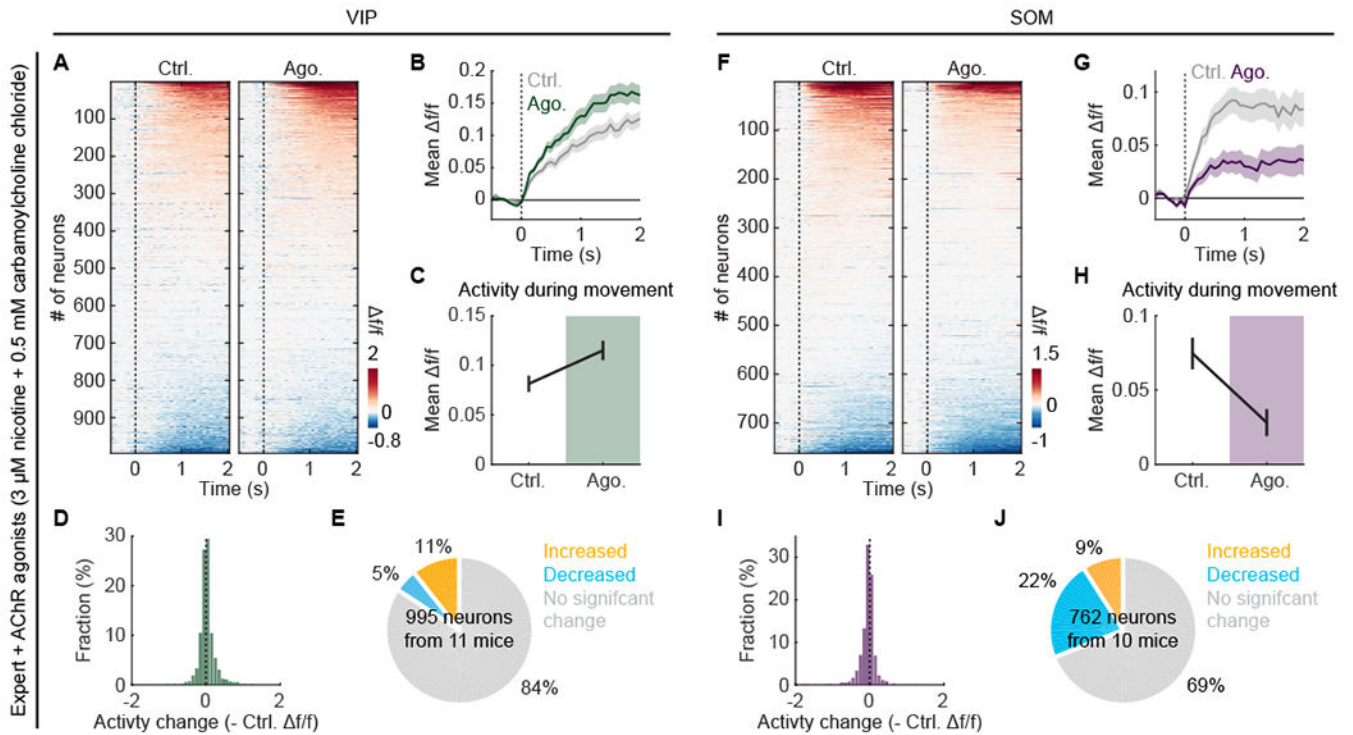
Figure 8. Pharmacological activation of cholinergic signaling increases VIP- and decreases SOM-IN activity during movements in expert mice

(A) Activity of VIP-INs in the right M1 at the expert stage aligned to the movement onset, with or without local applications of AChR agonist (995 VIP-INs from 11 mice). Each row represents the activity averaged across trials of individual neurons, sorted according to their activity level during movements within each session. Ctrl.: control sessions, Ago.: manipulation sessions with AChR agonists.

(B) Activity of VIP-INs averaged across movements and neurons in control and manipulation sessions aligned to the movement onset (mean ± SEM).

(C) Activity during movements averaged across VIP-INs in control and manipulation sessions (p = 0.0063, mixed-effects model, mean ± SEM).

(D) Distribution of changes in the activity level of VIP-INs during movements in the manipulation session compared to the control session.

(E) Fraction of VIP-INs with significant changes in the activity level during movements in the manipulation session compared to the control session at the naive stage..

(F)-(J) Same as (A)-(E) but for SOM-INs (762 SOM-INs from 10 mice). For (H), AChR agonists decreased the activity of SOM-INs in expert animals (p = 0.0166, mixed-effects model, mean ± SEM). See also Figure S8.

REAGENT or RESOURCE	SOURCE	IDENTIFIER
Fiji	Schindelin et al., 2012	RRID: SCR_002285
LabView	National Instruments	RRID: SCR_014325
Bpod	Sanworks	https://sites.google.com/site/bpoddocumentation/home?authuser=0
Arduino IDE	Arduino	https://www.arduino.cc/en/software
HCImage Live	Hamamatsu	RRID: SCR_015041
ScanImage	Vidrio Technologies	RRID: SCR_014307
IC Capture	The Imaging Source	RRID: SCR_016047
Zen	Zeiss	RRID: SCR_013672
JADER	Cardoso, 1999	https://www.mathworks.com/matlabcentral/mlc-downloads/downloads/submissions/67527/versions/3/previews/jadeR.m/index.html
ridgeMML	Karabatsos, 2018; Musall et al., 2019	http://churchlandlab.labsites.cshl.edu/code
Custom MATLAB code	This paper	https://github.com/CRen2333/InhibitoryNeuron_LeverPress.git
Other		
Axio Zoom. V16	Zeiss	https://www.zeiss.com/microscopy/int/products/stereo-zoom-microscopes/axio-zoom-v16.html
Illuminator HXP 200C	Zeiss	435716-0000-000
ORCA-Flash4.0 V2	Hamamatsu	https://www.hamamatsu.com/us/en/product/cameras/cmos-cameras.html
Movable objective microscope (MOM)	Sutter Instrument	RRID: SCR_018860
B-Scope	Thorlabs	https://www.thorlabs.com/thorproduct.cfm?partnumber=B-SCOPE
Ti:Sapphire laser (Mai Tai HP)	Newport	MTEV HP1040S
Monochrome industrial camera	The Imaging Source	DMK 23U618
TV lens (35mm f/1.7)	Fujian	https://www.amazon.com/Fujian-Mount-Camera-Adapter-bundle/dp/B075RZT7P8
Green laser 532 nm	Shanghai Laser & Optics Century	GL532T3
Arduino	Arduino	https://www.arduino.cc/